


Underlying physics of mixing efficiency for shear-forced, stratified turbulence

Young R. Yi * and Jeffrey R. Koseff

Bob and Norma Street Environmental Fluid Mechanics Laboratory,

Department of Civil and Environmental Engineering, Stanford University, Stanford, California 94305, USA



(Received 15 March 2023; accepted 31 July 2023; published 23 August 2023)

We study three types of homogeneous, shear-forced, stably stratified turbulence in a triply periodic domain over a wide range of stratification strengths. The shear forcings correspond to three different turbulence generation scenarios: (i) vertically sheared mean horizontal flow, (ii) horizontally sheared mean vertical flow, and (iii) horizontally sheared mean horizontal flow. At all stratification strengths, i.e., from weak to strong, we observe a persistent ordering of the mixing coefficient Γ values such that the second set of simulations exhibit the largest values and the third set of simulations exhibit the smallest values, implying that the turbulence generation mechanism has a significant effect on Γ . For very strong stratification, we observe that Γ begins to decrease, and this shift is associated with the difference between the vertical component of turbulent kinetic energy and turbulent potential energy becoming negative and the pressure scrambling term increasing in magnitude to keep the vertical buoyancy flux positive. Our findings demonstrate that the turbulence generation mechanism strongly affects the mixing characteristics of stably stratified turbulence and parametrizations of Γ for climate applications will need to distinguish how the turbulence is generated, which will require knowing more information than just the buoyancy Reynolds number Re_b and the turbulent Froude number Fr_k .

DOI: [10.1103/PhysRevFluids.8.084803](https://doi.org/10.1103/PhysRevFluids.8.084803)

I. INTRODUCTION

The fluid motions of earth's oceans are characterized by a large range of spatial and temporal scales [1,2]. Because it is simply not possible to resolve all these scales, global ocean simulations often rely on downgradient closures to represent subgrid-scale (unresolved) turbulent momentum and scalar fluxes [3,4]. Unfortunately, the vertical density distribution and meridional transport of large-scale ocean simulations are sensitive to the choice of subgrid-scale models [5–9]. In particular, vertical buoyancy fluxes for large-scale ocean simulations are often calculated from a flux parametrization using a turbulent diffusivity following Ref. [10]. A nondimensional form from Ref. [11] is

$$\frac{D_T}{D} = \left(\frac{Ri_f}{1 - Ri_f} \right) \frac{\epsilon_k}{DN^2} = \Gamma \left(\frac{\epsilon_k}{\nu N^2} \right) \left(\frac{\nu}{D} \right) = \Gamma Re_b Pr, \quad (1)$$

where D_T and D are the turbulent and molecular diffusivities of the stratifying scalar, respectively; Ri_f is the mixing efficiency (also known as the flux Richardson number), generally representing the fraction of the energy input that is used to irreversibly mix the stratifying scalar field; $\Gamma = Ri_f/(1 - Ri_f)$ is the mixing coefficient (also known as the flux coefficient); ϵ_k is the dissipation rate of turbulent kinetic energy; ν is the kinematic viscosity of the fluid; $N^2 = -(g/\rho_0)d_z\bar{\rho}$ is the vertical background stratification; $Re_b = \epsilon_k/\nu N^2$ is the buoyancy Reynolds number, which is a

*yryi@stanford.edu

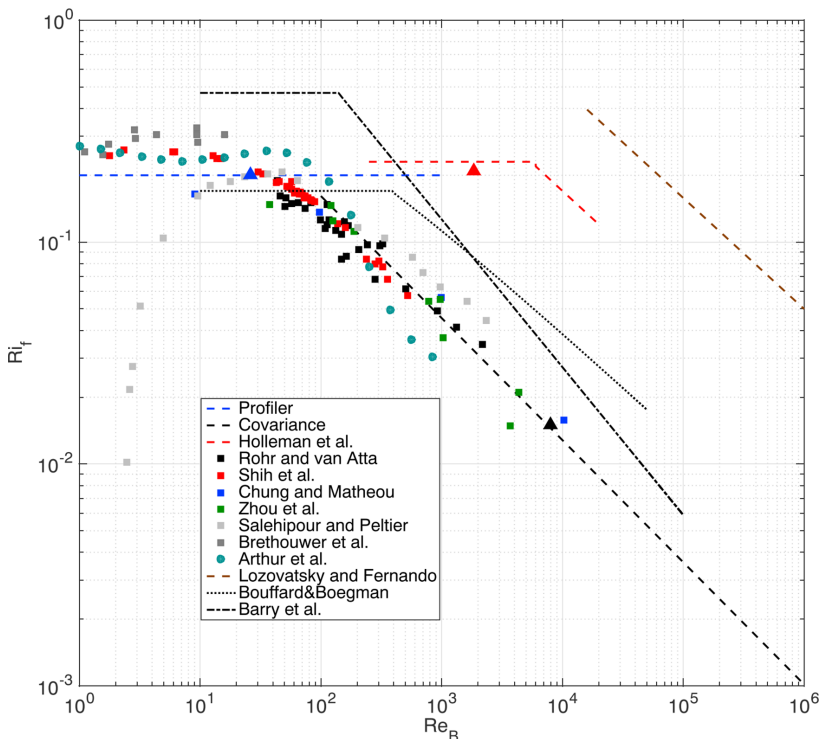


FIG. 1. Mixing efficiency Ri_f as a function of buoyancy Reynolds number Re_b from Monismith *et al.* [18]. The legend specifies the denotations for data from the following sources: (i) (Profiler dataset) measurements from the NATRE, BBTRE96/97, SPAM1/2, MIXET2, EXITS1, and GRAVILUCK campaigns that were accessed via the NSF supported microstructure database curated by Dr. Amy Waterhouse and Prof. Jennifer MacKinnon [19]; (ii) (Covariance dataset) measurements presented in Refs. [20–23]; and (iii) Refs. [11,24–33]. (The figure has been reproduced in agreement with AGU permissions policy for republication in academic works.)

measure of the intensity of a stratified turbulent flow; and $Pr = \nu/D$ is the molecular Prandtl number. While several definitions of the flux Richardson number exist, we will mainly use the reversible and irreversible definitions in our analyses, i.e., $Ri_{f,r} = B/P_k$ and $Ri_f = \epsilon_p/(\epsilon_k + \epsilon_p)$, respectively, where ϵ_p is the dissipation rate of turbulent potential energy, B is the vertical buoyancy flux, and P_k is the rate of production of turbulent kinetic energy. For statistically stationary and homogeneous turbulence, these two definitions are equivalent since $B = \epsilon_p$ and $P_k = \epsilon_k + \epsilon_p$ under these conditions, but there are important differences between the two definitions when the turbulent flow is unsteady and inhomogeneous. Reference [12] provides further discussion and quantitative comparisons of the different definitions of the flux Richardson number and Ref. [13] introduces a generalized definition of the mixing efficiency for unsteady, inhomogeneous, stably stratified turbulent flows.

Given that the molecular Prandtl number is known and the buoyancy Reynolds number can be calculated from parameters measurable in the field, the main challenge of using Eq. (1) is estimating Γ in terms of easily accessible quantities. This task has been summarized well in Refs. [14–17]. Here we provide a brief sketch of more recent efforts to estimate Γ . Reference [18] analyzed the relationship between Ri_f and Re_b using a large collection of laboratory experiments, field measurements, and numerical simulations of different types of stably stratified turbulent flows. The study found that most data sets exhibited a constant value of Ri_f for $Re_b < 100$ and $Ri_f \sim Re_b^{-1/2}$ for $Re_b > 100$ with some data sets exhibiting this transition at values of Re_b much larger than 100

(see Fig. 1, reproduced from Ref. [18]). Another set of efforts to address this challenge has involved studying the relationship between Γ and the turbulent Froude number $Fr_k = \epsilon_k/Nk$, where k is the turbulent kinetic energy (TKE). While Re_b accounts for the strength of the background stratification through N , the same value of Re_b can be achieved by both weakly and strongly stratified conditions with the appropriate turbulence levels. By considering that the buoyancy Reynolds number can be rewritten as $Re_b = Re_L Fr_k^2$, where $Re_L = k^2/\nu\epsilon_k$ is the large-eddy Reynolds number, Ref. [34] importantly showed that Γ depends primarily on Fr_k and exhibits a weaker dependence on the Reynolds number. Reference [35] also observed this primary dependence on Fr_k for sheared, stably stratified turbulence, where $\Gamma \approx \text{const}$ was found as Re_b was increased across approximately two orders of magnitude. Other recent work [36–40] has also demonstrated a strong relationship between Γ and Fr_k . Furthermore, Ref. [41] extended this Fr_k -based description of Γ in Ref. [36] to explicitly account for the effects of mean shear through a nondimensional shear parameter $S_* = Sk/\epsilon_k$.

While obtaining field estimates of k is challenging, estimating Γ using Fr_k does seem to alleviate the issue of nonunique regime transitions when considering $\Gamma = f(Re_b)$ (see, e.g., Figs. 14 and 6 of Ref. [38]). Nevertheless, there still remains the question of how the turbulence generation mechanism affects the magnitude of Γ for fixed values of Fr_k . Considering Fig. 2 of Ref. [18] once more (see Fig. 1), perhaps some of the differences for $Re_b < 100$ could be explained by the fact that different turbulence generation mechanisms are at play. Additionally, Fig. 1 of Ref. [36] also exhibits a lack of complete collapse between the sheared and unsheared data sets, further suggesting the importance of distinguishing different turbulence generation mechanisms. For example, Ref. [37] found Γ values varying by roughly 30% at $Fr_k \approx 10^{-2}$, and this type of forcing sensitivity has been observed too in sheared stably stratified turbulence (see, e.g., Ref. [41] for a homogeneous example and Ref. [42] for an inhomogeneous example contrasting Kelvin-Helmholtz and Holmboe systems). Finally, when considering buoyancy-driven systems (another type of stratified flow) very efficient mixing is expected (see, e.g., Ref. [43,44]) relative to mechanically driven systems at similar values of Fr_k , further illustrating the importance of the turbulence generation mechanism.

To explore the relationship between turbulence generation mechanisms and the values of the mixing efficiency, we extend the work of Ref. [40] by considering shear-forced, stably stratified turbulence given that turbulent oceanic processes generally involve the combined effects of shear and stratification. Reference [40] studied forced (unsheared), stably stratified turbulence, where the shape of the mixing coefficient curve as a function of Fr_k was connected to important changes in the Reynolds stress and buoyancy flux budgets, in particular to (i) when the pressure-strain correlations became the dominant generation mechanism for the vertical Reynolds stresses and (ii) the pressure scrambling term, which involves correlation between the pressure fluctuations and vertical gradient of the density fluctuations, switched signs.

Generally, the shear production term associated with the TKE equation can be written as $P_k = -\overline{u'_i u'_j \partial_j \bar{u}_i}$, where k denotes that this quantity is associated with TKE and is not a tensor index. In this expression, $i, j = 1, 2, 3$ are the tensor indices and repeated indices imply summation. Here we consider three shear forcing scenarios with respect to a vertical background stratification: (i) vertical shear of mean streamwise velocity ($P_k = -\overline{u'w' \partial_z \bar{u}}$), (ii) streamwise shear of mean vertical velocity ($P_k = -\overline{w'u' \partial_x \bar{w}}$), and (iii) lateral shear of mean streamwise velocity ($P_k = -\overline{u'v' \partial_y \bar{u}}$). A schematic of these three scenarios is shown in Fig. 2, where the colored shading represents the stable background stratification and the arrows indicate the mean profiles associated with each type of shear forcing.

Without vertical stratification, these three cases could be made equivalent under appropriate coordinate transformations, but they become distinct when there is vertical stratification. For example, while the first and third scenarios directly generate the streamwise Reynolds stresses ($\overline{u'u'}$) and the second scenario directly generates the vertical Reynolds stresses ($\overline{w'w'}$), all three of these scenarios convert the vertical Reynolds stresses into turbulent potential energy via the vertical buoyancy flux ($g\overline{w'\rho'}/\rho_0$). The first type of shear forcing is connected to turbulence associated with shear layers

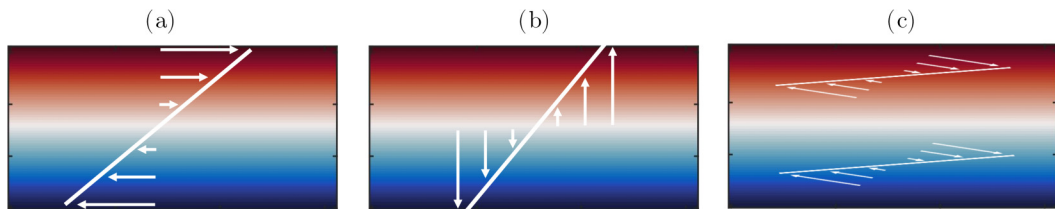


FIG. 2. Schematic of the three types of shear-forced, stably stratified turbulence scenarios. (a) Set 1: $d_z \bar{u}$ ($f_x = -w' d_z \bar{u}$), vertical shear of mean streamwise velocity. (b) Set 2: $d_x \bar{w}$ ($f_z = -u' d_x \bar{w}$), streamwise shear of mean vertical velocity. (c) Set 3: $d_y \bar{u}$ ($f_x = -v' d_y \bar{u}$), lateral shear of mean streamwise velocity. The colored shading represents the stable background stratification.

and stratified channel flows [8,26,38,42,45–57]. The second type of shear forcing is connected to turbulence associated with inclined gravity currents, obliquely propagating internal gravity waves, and turbulent plumes [58–63]. The third type of shear forcing is connected to turbulence associated with lateral shear [64–71]. The numerous shear-driven turbulent mixing processes in the global oceans (see, e.g., Fig. 5 of Ref. [72] and Fig. 1 of Ref. [73]) are likely represented by some combination of these three scenarios.

Here we conduct a set of direct numerical simulations (DNSs) of these three different types of shear-forced, stably stratified, homogeneous turbulence with the goal of studying the Reynolds stress and scalar flux dynamics as a function of the relative importance of mean shear and stratification. Our goals are twofold: (i) study how the different shear configurations (i.e., large-scale forcing) affect the mixing coefficient as a function of increasing stratification and (ii) explain the differences in the mixing coefficient for the three forcing scenarios by identifying the driving physical mechanisms for the Reynolds stresses and scalar fluxes.

This paper is organized as follows. Governing equations, related second-moment equations, and solution methodology are discussed in Sec. II. Simulation results as a function of Fr_k and an alternative formulation of Ri_f with some remarks on Reynolds-number effects are presented in Sec. III. A summary and a discussion of our results are provided in Sec. IV.

II. PROBLEM SETUP AND METHODOLOGY

A. Equations of motion and second-moment budgets

In this study we use the incompressible Navier-Stokes equations under the Boussinesq approximation with linear velocity forcing [74]

$$\frac{\partial u_j}{\partial x_j} = 0, \quad (2)$$

$$\frac{\partial u_j}{\partial t} + u_m \frac{\partial u_j}{\partial x_m} = -\frac{1}{\rho_0} \frac{\partial p}{\partial x_j} - \frac{g}{\rho_0} \rho \delta_{j3} + \nu \frac{\partial^2 u_j}{\partial x_m \partial x_m} + f_j, \quad (3)$$

$$\frac{\partial \rho}{\partial t} + u_m \frac{\partial \rho}{\partial x_m} = -w \frac{d\bar{\rho}}{dz} + D \frac{\partial^2 \rho}{\partial x_m \partial x_m}, \quad (4)$$

where u_j , p , and ρ represent velocity, pressure, and density fluctuations, respectively; $\bar{\rho}(z)$ is the stable, linearly varying, background density field ($d_z \bar{\rho} < 0$); g is the gravitational acceleration; ρ_0 is the reference density; ν is the kinematic viscosity of the fluid; D is the molecular diffusivity of density; and $f_j = A_{jm} u_m$ is a forcing term that depends linearly on the velocity based on a second-rank tensor A_{jm} , whose entries are constant in time and uniform in space. Tensor indices 1, 2, and 3 correspond to spatial directions x , y , and z and velocity fields u , v , and w , respectively, with gravity acting along the z axis. Repeated indices imply summation.

The turbulent kinetic energy $k = \frac{1}{2}\overline{u_j u_j}$, turbulent potential energy (TPE) $k_p = \frac{1}{2}\alpha^2 \overline{\rho \rho}$, Reynolds stress (RS) $\overline{u_i u_j}$, and density flux (DF) $\overline{u_j \rho}$ equations associated with (2)–(4) are (BF denotes buoyancy flux)

$$\frac{dk}{dt} = \underbrace{\overline{u_j f_j}}_{\text{TKE production}} - \underbrace{\frac{g}{\rho_0} \overline{w \rho}}_{\text{BF}} - \underbrace{v \frac{\partial \overline{u_j}}{\partial x_m} \frac{\partial \overline{u_j}}{\partial x_m}}_{\text{TKE dissipation}} = P_k - B - \epsilon_k, \quad (5)$$

$$\frac{dk_p}{dt} = \underbrace{\frac{g}{\rho_0} \overline{w \rho}}_{\text{BF}} - \underbrace{D\alpha^2 \frac{\partial \overline{\rho}}{\partial x_m} \frac{\partial \overline{\rho}}{\partial x_m}}_{\text{TPE dissipation}} = B - \epsilon_p, \quad (6)$$

$$\begin{aligned} \frac{d\overline{u_i u_j}}{dt} &= \underbrace{(\overline{u_i f_j} + \overline{u_j f_i})}_{\text{RS production}} + \underbrace{\frac{2}{\rho_0} \overline{p s_{ij}}}_{\text{pressure strain}} - \underbrace{\frac{g}{\rho_0} (\overline{u_i \rho} \delta_{j3} + \overline{u_j \rho} \delta_{i3})}_{\text{RS source or sink due to BF}} - \underbrace{2v \frac{\partial \overline{u_i}}{\partial x_m} \frac{\partial \overline{u_j}}{\partial x_m}}_{\text{RS dissipation}} \\ &= P_{ij} + R_{ij} - B_{ij} - \epsilon_{ij}, \end{aligned} \quad (7)$$

$$\begin{aligned} \frac{d\overline{u_j \rho}}{dt} &= \underbrace{\overline{f_j \rho}}_{\text{DF production}} + \underbrace{\frac{1}{\rho_0} \overline{p \frac{\partial \rho}{\partial x_j}}}_{\text{pressure scrambling}} - \underbrace{\overline{u_j w} \frac{d\overline{\rho}}{dz} - \frac{g}{\rho_0} \overline{\rho \rho} \delta_{j3}}_{\text{DF source or sink due to RS and TPE}} - \underbrace{(v + D) \frac{\partial \overline{u_j}}{\partial x_m} \frac{\partial \overline{\rho}}{\partial x_m}}_{\text{DF dissipation}}, \end{aligned} \quad (8)$$

where $s_{ij} = \frac{1}{2}(\partial_j u_i + \partial_i u_j)$ is the rate-of-strain tensor associated with the velocity fluctuations and $\alpha = g/\rho_0 N$ is a constant and uniform dimensional factor (N is also constant and uniform) needed to convert the dimensions of density to those of velocity. In (5) and (6), P_k is the rate of production of TKE from linear forcing, B is the buoyancy flux, and ϵ_k and ϵ_p are the dissipation rates of TKE and TPE, respectively. We note that the subscripts k and p indicate quantities associated with TKE and TPE, respectively, and do not indicate tensor indices. In (7), P_{ij} is the rate of production of the Reynolds stresses from linear forcing, R_{ij} represents the pressure-strain correlations, B_{ij} is a term associated with the buoyancy flux, and ϵ_{ij} represents the dissipation rates of the Reynolds stresses. In (8), the first term on the right-hand side (RHS) is a production term associated with the linear forcing. The second term on the RHS represents correlations between the pressure and the density gradient and is often referred to as the pressure scrambling term in analogy to the pressure-strain correlations that redistribute or scramble the diagonal Reynolds stresses [75,76]. Physically, for passive scalar fluxes, the pressure scrambling term has been shown to be the primary mechanism that balances the terms involving the mean shear and mean scalar gradients [77]. The third and fourth terms on the RHS represent sources and sinks due to the Reynolds stresses and TPE, and the final term on the RHS is a dissipation term. We use overlines to denote volume averaging, and because our flow is statistically homogeneous in all three spatial directions, the transport terms are exactly zero, leaving only the volume-averaged source and sink terms in (5)–(8).

To study the three distinct shear-forcing scenarios as illustrated in Fig. 2, we consider these three choices of the linear forcing term: $f_j = A_{13} w \delta_{j1} = -w d_z \overline{u} \delta_{j1}$ for the first case, $f_j = A_{31} u \delta_{j3} = -u d_x \overline{w} \delta_{j3}$ for the second case, and $f_j = A_{12} v \delta_{j1} = -v d_y \overline{u} \delta_{j1}$ for the third case. In the subsequent sections, we denote all three forcing rates A_{13} , A_{31} , and A_{12} by $-S$, but we highlight their differences in Table I by summarizing the volume-averaged terms involving f_j in (5)–(8). In Sec. III we evaluate the terms on the RHSs of (5)–(8) as a function of the turbulent Froude number for each of the three shear-forcing scenarios. This allows us to explore how different turbulence generation mechanisms lead to different large-scale anisotropy based on how energy is transferred between the three components of TKE and TPE and, as a result, how this leads to differences in the mixing coefficient values across the three scenarios.

Before moving to the methods, we note that Eqs. (2)–(4) do not involve any mean advection terms. To distinguish this system from the classical homogeneous shear turbulence that does include mean advection, we will refer to it as the shear-forced model problem. If mean advection terms were

TABLE I. Summary of terms involving the forcing in Eqs. (5)–(8).

Term	Set 1 ($d_z \bar{u}$)	Set 2 ($d_x \bar{w}$)	Set 3 ($d_y \bar{u}$)
Forcing			
$f_j = A_{jm} u_m$	$f_1 = A_{13} w = -w d_z \bar{u}$	$f_3 = A_{31} u = -u d_x \bar{w}$	$f_1 = A_{12} v = -v d_y \bar{u}$
TKE production			
$P_k = \overline{u_j f_j}$	$P_k = \overline{u_1 f_1} = -\overline{u w} d_z \bar{u}$	$P_k = \overline{u_3 f_3} = -\overline{w u} d_x \bar{w}$	$P_k = \overline{u_1 f_1} = -\overline{u v} d_y \bar{u}$
Diagonal Reynolds stress production			
$P_{ij} = \overline{u_i f_j} + \overline{u_j f_i}$ (for $i = j$)	$P_{11} = 2P_k = -2\overline{u w} d_z \bar{u}$	$P_{33} = 2P_k = -2\overline{w u} d_x \bar{w}$	$P_{11} = 2P_k = -2\overline{u v} d_y \bar{u}$
Reynolds shear stress production			
$P_{ij} = \overline{u_i f_j} + \overline{u_j f_i}$ (for $i \neq j$)	$P_{13} = P_{31} = -\overline{w w} d_z \bar{u}$	$P_{13} = P_{31} = -\overline{u u} d_x \bar{w}$	$P_{12} = P_{21} = -\overline{v v} d_y \bar{u}$

present, the second forcing scenario would require a source term in Eq. (4) to counteract the tilt of the mean vertical stratification similarly as in Ref. [78]. Furthermore, when the mean advection terms are missing, there is a modified prefactor in the Poisson equation for the pressure fluctuations, which affects the volume-averaged pressure-strain correlations and consequently changes the relative magnitudes of the Reynolds stresses compared to their classical counterparts (see Tables 1 and 2 of Ref. [74]). While the two systems will also differ in how flow features are deformed and their transition to turbulence (see, e.g., Refs. [47–49]), Ref. [41] demonstrated that both model problems exhibit similar power-law scaling relationships between Γ and turbulence parameters just with different proportionality constants. This is likely due to the volume-averaged Reynolds stress and buoyancy flux equations being the same for the two systems. As a first consideration, we believe the study of these three shear-forced systems reveals important insights regarding the relationship between the turbulence generation mechanism and the mixing coefficient that will extend to systems with mean advection.

B. Numerical solution procedure and nondimensional parameters

We solved Eqs. (2)–(4) for a triply periodic cubic domain of length $L = 2\pi$ using our own Fourier pseudospectral solver with a fourth-order Runge-Kutta time-stepping scheme. We verified the fourth-order temporal accuracy and nonlinear advection terms by comparing our numerical solutions with the analytical solutions of a decaying Taylor-Green vortex in two dimensions [79]. We also dealiased the nonlinear terms exactly by zero padding [80]. Finally, we implicitly verified the linear shear forcing and density coupling by observing that our simulations obeyed the volume- and time-averaged turbulence budgets shown in Eqs. (5)–(8) (see Figs. 4, 7, 8, 12, and 13). A series of rectangular domain simulations with $L_x = 2L_y = 2L_z = 4\pi$ was carried out for the first type of forcing (vertical shear of mean horizontal flow) to explore domain size effects for shear-forced, stably stratified turbulence simulations, which were found to be insignificant for the quantities of interest in this study [41]. Therefore, the remaining simulations (i.e., second and third forcing scenarios) were conducted just using cubic domains of length $L = 2\pi$. Additional information about the three sets of simulations is provided in Table II.

The nondimensional input parameters of our system are N/S , SL^2/ν , and $\text{Pr} = \nu/D$, where N is the mean buoyancy frequency and S is the rate of shear forcing (they are both constant in time and uniform in space). For our simulations, we prescribed a molecular Prandtl number of unity and we primarily varied N/S to study the effects of increasing stable stratification relative to momentum forcing. Because the value of S varied across our simulations, our input

TABLE II. Global input parameters for the numerical simulations. Simulations S1C1–S1C6, S1R16, S2C19–S2C23, and S3C21–S3C28 (see Tables III–V) used $\Delta t = 1.25 \times 10^{-3}$ s for numerical stability (C denotes cubic and R rectangular).

Domain	L_x, L_y, L_z (m)	N_x, N_y, N_z	Δt (s)	ν (m ² /s)	κ (m ² /s)	g (m ² /s)	ρ_0 (kg/m ³)
			Set 1				
Cubic	$2\pi, 2\pi, 2\pi$	64, 64, 64	2.5×10^{-3}	5×10^{-2}	5×10^{-2}	9.8	1
Rectangular	$4\pi, 2\pi, 2\pi$	128, 64, 64	2.5×10^{-3}	5×10^{-2}	5×10^{-2}	9.8	1
			Set 2				
Cubic	$2\pi, 2\pi, 2\pi$	64, 64, 64	2.5×10^{-3}	5×10^{-2}	5×10^{-2}	9.8	1
			Set 3				
Cubic	$2\pi, 2\pi, 2\pi$	64, 64, 64	2.5×10^{-3}	5×10^{-2}	5×10^{-2}	9.8	1

Reynolds number SL^2/ν also varied. The nondimensional output parameters of interest of our system are $\text{Re}_b = \epsilon_k/\nu N^2 = (l_O/\eta_k)^{4/3}$, $\text{Re}_S = \epsilon_k/\nu S^2 = (l_C/\eta_k)^{4/3}$, $\text{Re}_L = k^2/\nu\epsilon_k = (l_L/\eta_k)^{4/3}$, $\text{Fr}_k = \epsilon_k/Nk = (l_L/l_O)^{-2/3}$, $S_* = Sk/\epsilon_k = (l_L/l_C)^{2/3}$, and $\Gamma = \epsilon_p/\epsilon_k$, where $l_L = k^{3/2}/\epsilon_k$, $l_O = (\epsilon_k/N^3)^{1/2}$, $l_C = (\epsilon_k/S^3)^{1/2}$, and $\eta_k = (v^3/\epsilon_k)^{1/4}$ are the large-eddy, Ozmidov, Corrsin, and Kolmogorov scales, respectively. The first five nondimensional parameters are the buoyancy Reynolds number, the shear Reynolds number, the large-eddy Reynolds number, the turbulent Froude number, and the nondimensional shear parameter and they can be interpreted as the ratio of turbulence length scales. We report the values of these parameters from our simulations as a function of the gradient Richardson number ($\text{Ri}_g = N^2/S^2$) in Tables III–V. We also provide the values of SL^2/ν as a function of Ri_g for all simulations. For the rectangular domain simulations of the first type of shear forcing, we have used $L_x = 4\pi$ instead of $L = 2\pi$ to compute the input Reynolds number.

III. RESULTS

A. Parameter space and total energy budget

We first study the nondimensional total energy budget by combining (5) and (6) under statistically stationary conditions. For the three forcing scenarios, we arrive at the following expressions:

$$\frac{N}{S} = -\frac{2b_{13}}{\text{Fr}_k(1 + \Gamma)}, \quad (9a)$$

$$\frac{N}{S} = -\frac{2b_{31}}{\text{Fr}_k(1 + \Gamma)}, \quad (9b)$$

$$\frac{N}{S} = -\frac{2b_{12}}{\text{Fr}_k(1 + \Gamma)}. \quad (9c)$$

Equations (9a)–(9c) are one particular manifestation of the nondimensional total energy budget that relates the input parameter N/S to output parameters b_{13} , b_{31} , b_{12} , Fr_k , and Γ , where $b_{ij} = \overline{u_i u_j}/2k - \delta_{ij}/3$ is the Reynolds stress anisotropy tensor. Because b_{ij} is symmetric, $b_{13} = b_{31}$, but we have distinguished them in Eqs. (9a) and (9b) to indicate that the expressions correspond to two different types of shear forcing. In Fig. 3(a) we plot the terms on the RHSs of Eqs. (9a)–(9c) as a function of the gradient Richardson number ($\text{Ri}_g = N^2/S^2$). Each symbol represents volume- and time-averaged values, and each color and symbol combination corresponds to one of the three forcing strategies: type 1 (red squares), type 2 (blue triangles), and type 3 (orange circles). The dashed lines represent $y = 2x^{1/2}$ (red), $y = 4x^{1/2}$ (blue), and $y = x^{1/2}$ (orange). The fact that all of the points lie close to the dashed lines indicates statistically stationary turbulence.

Next we focus on the relationship between Ri_g , which is prescribed in our simulations, and the turbulent Froude number Fr_k and the nondimensional shear parameter S_* , which are outcomes of our

TABLE III. Nondimensional parameters for the set of DNSs with the first type of shear forcing.

Simulation	Ri_g	SL_x^2/ν	Fr_k^a	S_*^a	Re_L^a	Re_b^a	Re_s^a	$\kappa_{max}\eta^a$
S1C1	1/1024	2368.71	13.43	2.38	183.64	37274.87	36.40	1.65
S1C2	1/512	2368.71	9.48	2.39	186.85	18711.79	36.55	1.65
S1C3	1/256	2368.71	6.66	2.40	177.25	8722.92	34.07	1.68
S1C4	1/128	2368.71	4.62	2.45	173.90	4164.84	32.54	1.70
S1C5	1/64	2368.71	3.21	2.49	175.48	1990.71	31.10	1.71
S1C6	1/32	4466.47	2.14	2.64	307.28	1540.23	48.13	1.12
S1C7	1/16	3158.27	1.42	2.81	189.00	418.93	26.18	1.55
S1C8	3/32	2578.72	1.10	2.97	115.02	154.08	14.44	1.99
S1C9	3/32	3947.84	1.09	2.98	191.37	262.72	24.63	1.41
S1C10	1/8	2233.24	0.89	3.18	92.77	83.66	10.46	2.33
S1C11	1/8	3947.84	0.87	3.24	159.27	134.44	16.81	1.55
S1C12	5/32	1997.47	0.75	3.39	64.05	39.77	6.21	2.79
S1C13	5/32	3947.84	0.72	3.52	135.54	76.01	11.88	1.68
S1C14	3/16	1823.43	0.66	3.48	49.70	24.44	4.58	3.15
S1C15	3/16	3947.84	0.62	3.70	120.99	49.93	9.36	1.78
S1C16	1/4	1579.14	0.54	3.72	34.67	11.65	2.91	3.81
S1C17	1/4	4737.41	0.50	3.99	117.78	32.14	8.03	1.70
S1C18	9/32	4466.47	0.46	4.10	117.38	26.70	7.51	1.78
S1C19	5/16	4237.27	0.42	4.23	101.56	20.02	6.26	1.91
S1C20	49/144	4737.41	0.39	4.35	122.23	21.00	7.15	1.75
S1C21	11/32	4040.08	0.39	4.36	103.74	17.20	5.91	1.98
S1C22	4/9	4737.41	0.32	4.72	121.60	13.55	6.02	1.83
S1C23	9/16	4737.41	0.27	4.91	132.94	11.47	6.45	1.81
S1C24	25/36	4737.41	0.23	5.31	148.50	8.83	6.13	1.85
S1R1	1/32	9474.82	2.20	2.57	252.15	1328.70	41.52	1.59
S1R2	1/16	9474.82	1.47	2.72	241.68	591.55	36.97	1.65
S1R3	3/32	11053.96	1.15	2.85	266.03	404.39	37.91	1.52
S1R4	1/8	11053.96	0.94	3.00	239.78	263.91	32.99	1.59
S1R5	5/32	11053.96	0.79	3.21	252.72	184.76	28.87	1.63
S1R6	3/16	12633.09	0.68	3.41	261.39	147.58	27.67	1.55
S1R7	1/4	12633.09	0.54	3.71	242.97	90.89	22.72	1.64
S1R8	9/32	12633.09	0.48	3.89	251.13	67.81	19.07	1.69
S1R9	5/16	14212.23	0.46	3.87	264.60	67.68	21.15	1.56
S1R10	11/32	14212.23	0.44	3.90	279.17	62.88	21.61	1.55
S1R11	4/9	14212.23	0.36	4.11	275.51	44.00	19.56	1.59
S1R12	9/16	15791.37	0.32	4.17	351.94	40.49	22.78	1.44
S1R13	25/36	18949.64	0.26	4.53	454.80	35.28	24.50	1.29
S1R14	121/144	18949.64	0.18	6.15	546.12	18.76	15.76	1.46
S1R15 ^b	17/20	18949.64	0.20	5.53	538.81	22.43	19.07	1.38
			0.18	6.05	524.70	19.03	16.18	1.46
S1R16 ^b	7/8	18949.64	0.18	5.99	532.85	17.85	15.62	1.44
			0.16	6.60	636.29	17.82	15.59	1.47
S1R17	9/10	18949.64	0.12	8.98	700.77	10.64	9.57	1.68
S1R18 ^b	1	18949.64	0.17	5.84	575.35	18.26	18.26	1.40
			0.14	6.90	673.25	16.21	16.21	1.51
			0.082	12.23	958.02	6.54	6.54	1.82
			0.058	17.12	1250.12	4.37	4.37	1.99

^aValues are volume and time averaged.

^bTime averaging has been carried out over multiple segments to avoid times when $Re_b < 1$.

TABLE IV. Nondimensional parameters for the set of DNSs with the second type of shear forcing.

Simulation	Ri_g	SL^2/ν	Fr_k^a	S_*^a	Re_L^a	Re_b^a	Re_S^a	$\kappa_{\max}\eta^a$
S2C1	1/1024	2368.71	13.20	2.42	186.23	35647.58	34.81	1.67
S2C2	1/512	2368.71	9.45	2.39	190.00	18902.92	36.92	1.65
S2C3	1/256	2368.71	6.65	2.41	185.52	9063.70	35.41	1.66
S2C4	1/128	2368.71	4.66	2.43	176.26	4257.34	33.26	1.69
S2C5	1/64	2368.71	3.27	2.45	193.66	2338.15	36.53	1.66
S2C6	1/32	2977.65	2.20	2.58	226.47	1245.96	38.94	1.45
S2C7	1/16	3158.27	1.50	2.67	234.66	613.88	38.37	1.42
S2C8	3/32	3223.40	1.17	2.78	242.54	416.19	39.02	1.41
S2C9	1/8	2791.55	0.97	2.93	190.37	229.48	28.69	1.64
S2C10	5/32	2996.20	0.79	3.21	207.15	156.99	24.53	1.63
S2C11	3/16	2735.15	0.71	3.27	154.50	101.91	19.11	1.84
S2C12	1/4	3158.27	0.55	3.61	168.34	66.16	16.54	1.76
S2C13	9/32	2977.65	0.52	3.62	162.52	52.79	14.85	1.86
S2C14	5/16	2824.85	0.48	3.75	126.87	36.34	11.36	2.05
S2C15	11/32	2693.38	0.46	3.72	123.32	32.71	11.24	2.10
S2C16	4/9	3553.06	0.37	4.04	151.67	24.24	10.77	1.83
S2C17	9/16	3947.84	0.31	4.28	168.83	19.39	10.91	1.74
S2C18	5/8	4737.41	0.27	4.74	193.28	16.28	10.17	1.62
S2C19	25/36	3947.84	0.19	6.23	157.83	7.67	5.33	2.16
S2C20	3/4	4737.41	0.22	5.17	199.40	11.98	8.99	1.69
S2C21	4/5	5132.19	0.16	6.97	230.45	7.00	5.60	1.83
S2C22	17/20	5132.19	0.17	6.28	241.34	8.48	7.21	1.74
S2C23	1	5132.19	0.16	6.12	248.63	7.94	7.94	1.69

^aValues are volume and time averaged.

simulations. Because N and S are both prescribed, the variations of Fr_k and S_* with Ri_g are entirely due to changes in k and ϵ_k . We can interpret the two outcome variables using timescale ratios such that $Fr_k \sim \tau_B/\tau_L$ and $S_* \sim \tau_L/\tau_S$, where $\tau_L \sim k/\epsilon_k$ is the large-eddy timescale, $\tau_B \sim 1/N$ is the buoyancy timescale, and $\tau_S \sim 1/S$ is the shear timescale. Since τ_L adjusts relative to τ_B and τ_S to achieve statistical stationarity, the changes to Fr_k and S_* can be understood as representing shifts in the strengths of mean stratification and mean shear relative to turbulence. In Fig. 3(b) we plot the volume- and time-averaged values of Fr_k and S_* with values of Ri_g shown in color such that $Ri_g = 1/4$ is shown in light gray. Once again, the symbols indicate the shear forcing strategy: type 1 (squares), type 2 (triangles), and type 3 (circles). Generally, we observe that S_* is insensitive to increasing Ri_g for $Fr_k > 1$. Physically, this indicates that the mean shear strength needed to sustain turbulence is not really affected by the background stratification. For $Fr_k < 1$, however, we observe large changes in S_* with respect to Fr_k as Ri_g is increased, indicating that stronger levels of mean shear are needed to sustain turbulence with increasing stratification. We also note that the first two types of forcing (squares and triangles) have similar values of S_* for any given value of Fr_k , but for $Ri_g > 1/4$ the third type of forcing (circles) typically has smaller values of S_* at a given Fr_k , suggesting that turbulence can be sustained at weaker levels of mean shear compared to the first two types of forcing.

B. The TKE and TPE budgets

We now turn to the steady-state and volume- and time-averaged TKE and TPE budgets, i.e., Eqs. (5) and (6). For all three types of forcing, the TKE budget (not shown) exhibits a balance between TKE production and the two sink terms (vertical buoyancy flux and dissipation) for all turbulent Froude numbers. Similarly, for all three types of forcing, the TPE budget (not shown)

TABLE V. Nondimensional parameters for the set of DNSs with the third type of shear forcing.

Simulation	Ri_g	SL^2/ν	Fr_k^a	S_*^a	Re_L^a	Re_b^a	Re_S^a	$\kappa_{\max}\eta^a$
S3C1	1/1024	1973.92	13.46	2.38	157.86	30980.61	30.25	1.89
S3C2	1/512	1973.92	9.56	2.37	147.61	15080.82	29.45	1.91
S3C3	1/256	1973.92	6.59	2.43	156.74	7392.60	28.88	1.91
S3C4	1/128	1973.92	4.71	2.40	157.97	3845.45	30.04	1.89
S3C5	1/64	1973.92	3.36	2.38	151.56	1897.69	29.65	1.90
S3C6	1/32	2368.71	2.30	2.45	180.65	1042.01	32.56	1.69
S3C7	1/16	2368.71	1.61	2.48	192.67	544.34	34.02	1.67
S3C8	3/32	2368.71	1.29	2.54	160.00	291.34	27.31	1.77
S3C9	1/8	3158.27	1.09	2.60	243.01	322.33	40.29	1.40
S3C10	3/16	3158.27	0.90	2.57	256.64	227.93	42.74	1.37
S3C11	1/4	3158.27	0.76	2.63	244.57	157.39	39.35	1.40
S3C12	3/8	3158.27	0.56	2.90	293.85	101.59	38.10	1.41
S3C13	1/2	3553.06	0.46	3.06	392.34	87.84	43.92	1.28
S3C14	5/8	3553.06	0.42	3.01	369.65	69.98	43.74	1.28
S3C15	3/4	3553.06	0.32	3.56	512.16	57.29	42.97	1.29
S3C16	7/8	3553.06	0.31	3.40	488.00	52.07	45.56	1.27
S3C17	1	3553.06	0.25	4.05	766.12	50.02	50.02	1.24
S3C18	9/8	3553.06	0.22	4.29	833.30	44.92	50.54	1.24
S3C19	5/4	3553.06	0.21	4.27	887.49	40.72	50.89	1.23
S3C20	3/2	3553.06	0.18	4.61	1028.29	35.19	52.79	1.22
S3C21	2	3553.06	0.14	5.22	1643.16	31.14	62.28	1.17
S3C22	5/2	3553.06	0.10	6.13	2176.53	24.04	60.10	1.18
S3C23	3	3553.06	0.090	6.42	2482.04	20.78	62.35	1.17
S3C24	4	3553.06	0.069	7.24	3732.01	18.03	72.12	1.13
S3C25	5	3553.06	0.052	8.58	4185.39	12.10	60.51	1.19
S3C26	6	3553.06	0.078	5.22	997.14	7.31	43.84	1.29
S3C27	7	3553.06	0.052	7.23	2540.65	9.12	63.87	1.17
S3C28	8	3553.06	0.034	10.50	4894.69	7.35	58.78	1.20

^aValues are volume and time averaged.

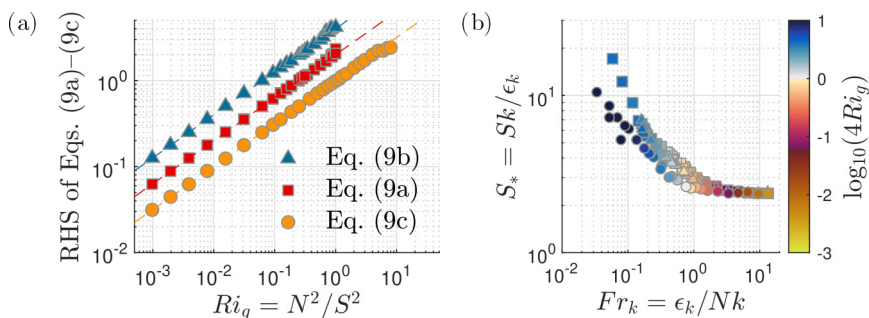


FIG. 3. (a) Plot of the RHSs of Eqs. (9a)–(9c) as a function of the gradient Richardson number Ri_g for the three forcing strategies: type 1 (red squares), type 2 (blue triangles), and type 3 (orange circles). The terms on the y axis have been calculated using volume- and time-averaged values. Data that lie along the dashed lines indicate statistically stationary turbulence. (b) Plot of the nondimensional shear parameter S_* as a function of the turbulent Froude number Fr_k with Ri_g shown in color such that $Ri_g = 1/4$ is shown in light gray. The symbol convention is the same as in (a).

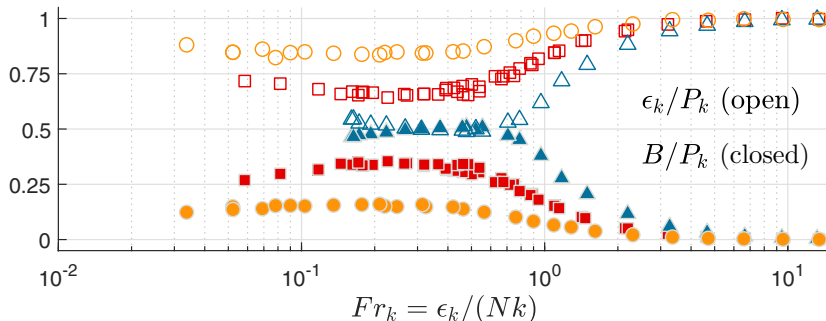


FIG. 4. Volume- and time-averaged values of the normalized buoyancy flux B (closed symbols) and TKE dissipation rate ϵ_k (open symbols). The color and symbol combinations correspond to the three shear forcing scenarios: type 1 (red squares), type 2 (blue triangles), and type 3 (orange circles).

exhibits a balance between the vertical buoyancy flux and TPE dissipation at all values of the turbulent Froude numbers. More interesting are the sink terms of the TKE budget (i.e., vertical buoyancy flux and TKE dissipation), which we plot as a function of the turbulent Froude number in Fig. 4 for the three types of forcing. The terms have been normalized by the TKE production so that they scale between values of 0 and 1. The vertical buoyancy flux is shown by closed symbols and the TKE dissipation is shown by open symbols.

First, we note that the two sink terms do in fact sum to unity, as expected for statistically stationary conditions. Second, we see that the peak magnitudes of the normalized vertical buoyancy fluxes are ordered such that the second (closed triangles) and third types of forcing (closed circles) exhibit the largest and smallest values, respectively, and the first type of forcing (red squares) exhibits intermediate values. This behavior will also be shown later by the peak magnitudes of the normalized vertical buoyancy flux for the three forcing types in Figs. 6(a2)–6(c2). The values of the normalized vertical buoyancy flux B/P_k can essentially be interpreted as representing the irreversible mixing efficiency $\text{Ri}_f = \epsilon_p/(\epsilon_k + \epsilon_p)$ given that $B = \epsilon_p$ and $P_k = \epsilon_k + \epsilon_p$ under statistically stationary conditions. Therefore, we observe that at a given value of Fr_k , the second type of forcing (blue) is most efficient ($\text{Ri}_{f,\text{max}} \approx 0.5$) and the third type of forcing (orange) is least efficient ($\text{Ri}_{f,\text{max}} \approx 0.2$) at irreversibly mixing the background density field. Finally, we note that all three types of forcing exhibit a range of turbulent Froude numbers over which the maximum value of B/P_k persists, but then at stronger stratifications ($\text{Fr}_k < 0.2$ for first and third forcing types and $\text{Fr}_k < 0.3$ for second forcing type), they all begin to exhibit less efficient mixing.

C. Characterization of turbulence anisotropy

In this section we focus on characterizing the turbulence anisotropy of the three different types of shear-forced, stably stratified turbulence. Additionally, we study the energetics that lead to the different large-scale anisotropy and connect our findings to the ordering of the mixing efficiency observed in Fig. 4.

1. Energy exchange diagrams

One way to think about the three types of shear-forced, stably stratified turbulence is to consider how turbulence is generated and eventually dissipated in the system. There are two sources of large-scale anisotropy: (i) shear forcing and (ii) buoyancy. For these three types of flows, the shear forcing directly produces only one component of TKE, which then leads to nonzero pressure correlations that drive indirect generation of the remaining two components. Next, because buoyancy force only acts in the vertical direction, the vertical component of TKE ($k_w = \overline{w\overline{w}}/2$) is further differentiated from the horizontal components ($k_u = \overline{u\overline{u}}/2$ and $k_v = \overline{v\overline{v}}/2$) by the fact

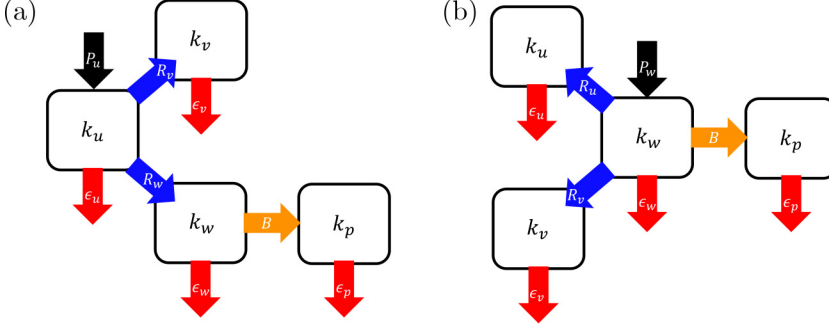


FIG. 5. Energy exchange diagrams corresponding to the three types of shear forcing: (a) first and third types of shear forcing and (b) second type of shear forcing. Ingoing arrows indicate sources and outgoing arrows indicate sinks of each of the four energy buckets under statistically stationary conditions. Black arrows indicate direct production by the forcing term. Blue arrows indicate the pressure-strain terms. Orange arrows indicate the buoyancy flux. Red arrows indicate the dissipation terms.

that the buoyancy flux directly converts k_w into k_p . The buoyancy force also indirectly affects the two horizontal components of TKE through the pressure-strain correlations since it modifies the pressure field via the pressure Poisson equation, which can be reached by taking the divergence of the momentum equations (3). In summary, shear forcing and buoyancy both directly affect the turbulence energetics through the production and buoyancy flux terms, respectively, and indirectly as well through the pressure-strain correlations.

We consider these ideas further by looking at the budgets for the streamwise, spanwise, and vertical components of the TKE (k_u , k_v , and k_w), which are given by the budgets for half of the diagonal Reynolds stresses [i.e., $i = j = 1, 2, 3$ components of Eq. (7)]. These budgets along with the budget for the vertical density flux [$\overline{w\rho}$, the $j = 3$ component of Eq. (8)] are provided below and they will be analyzed in greater detail in the following sections:

$$\frac{dk_u}{dt} = \overline{uf_1} + \frac{1}{\rho_0} \overline{ps_{11}} - \nu \overline{\frac{\partial u}{\partial x_m} \frac{\partial u}{\partial x_m}} = P_u + R_u - \epsilon_u, \quad (10)$$

$$\frac{dk_v}{dt} = \overline{vf_2} + \frac{1}{\rho_0} \overline{ps_{22}} - \nu \overline{\frac{\partial v}{\partial x_m} \frac{\partial v}{\partial x_m}} = P_v + R_v - \epsilon_v, \quad (11)$$

$$\frac{dk_w}{dt} = \overline{wf_3} + \frac{1}{\rho_0} \overline{ps_{33}} - \frac{g}{\rho_0} \overline{w\rho} - \nu \overline{\frac{\partial w}{\partial x_m} \frac{\partial w}{\partial x_m}} = P_w + R_w - B - \epsilon_w, \quad (12)$$

$$\frac{d\overline{w\rho}}{dt} = \overline{f_3\rho} + \frac{1}{\rho_0} \overline{p \frac{\partial \rho}{\partial z}} - \overline{ww} \frac{d\overline{\rho}}{dz} - \frac{g}{\rho_0} \overline{\rho\rho} - (\nu + D) \overline{\frac{\partial w}{\partial x_m} \frac{\partial \rho}{\partial x_m}}. \quad (13)$$

In Eqs. (10)–(12) the subscripts u , v , and w indicate quantities associated with the streamwise, spanwise, and vertical components of TKE, respectively, and do not indicate tensor indices. The production terms are denoted by P_u , P_v , and P_w ; the pressure-strain correlations are denoted by R_u , R_v , and R_w ; and the dissipation terms are denoted by ϵ_u , ϵ_v , and ϵ_w .

Qualitatively, we can visualize the energy exchange in our systems under statistically stationary conditions using the diagrams in Fig. 5. Ingoing arrows indicate sources and outgoing arrows indicate sinks of each of the four energy buckets. For the first and third types of forcing, k_u is directly produced (black arrow labeled P_u), while for the second type of forcing, k_w is directly produced (black arrow labeled P_w). Next the pressure-strain correlation terms redistribute some of this energy to the two components without direct generation mechanisms (i.e., k_v and k_w for types 1 and 3 and k_u and k_v for type 2), which are shown by the blue arrows labeled with R_u , R_v , and R_w . Then, for all three forcing types, some of k_w is transformed into k_p through the buoyancy flux

(orange arrow labeled B), and finally, dissipation acts as a sink for the three components of TKE and TPE (red arrows labeled ϵ_u , ϵ_v , ϵ_w , and ϵ_p). Once again, we highlight that R_u , R_v , and R_w are affected by the buoyancy field via the pressure Poisson equation and their net effect is to reduce the anisotropy among the three components of TKE that are due to the shear forcing and buoyancy.

Recall from Fig. 4 that the values of the mixing efficiency B/P_k are ordered based on the type of shear forcing with type 2 forcing having the largest values and type 3 forcing having the smallest. Because the buoyancy flux directly connects k_w and k_p , we might expect type 2 forcing, which involves direct production of k_w , to be associated with the largest buoyancy fluxes. Next, while both types 1 and 3 forcing have indirect generation of k_w , we note that type 1 forcing couples the streamwise and vertical directions through $\overline{uw} \neq 0$, whereas type 3 couples the streamwise and spanwise directions through $\overline{vw} \neq 0$. Therefore, we suspect that type 1 forcing could be more effective in generating k_w and converting it to k_p than type 3 forcing. We quantitatively explore these ideas in the subsequent sections.

2. Normal Reynolds stresses

As the degree of stable stratification increases relative to the momentum forcing (larger N relative to S), the turbulence becomes increasingly anisotropic due to the enhanced damping of vertical velocity fluctuations. The three types of forcing, however, interact with the vertical background stratification differently. We quantify this in Figs. 6(a1)–6(c1) by plotting the mean-square streamwise (circles), spanwise (squares), and vertical (triangles) velocity fluctuations versus the turbulent Froude number for the three types of shear-forcing simulations. The overlines denote volume and time averaging, and all three squared velocity components have been normalized by twice the TKE.

First, we note that the streamwise component of TKE (circles) is directly generated for the first and third types of forcing [Figs. 6(a1) and 6(c1)]. As a result, this component is the dominant contributor to TKE. Analogously, the vertical component of TKE (triangles) is directly generated for the second type of forcing [Fig. 6(b1)]. As a result, this component is largest for weak and moderate stratification strengths, but surprisingly, the streamwise component (circles), which is indirectly generated by pressure-strain correlations, becomes equally important at $Fr_k \approx 0.3$ and eventually surpasses the vertical component for $Fr_k < 0.3$.

While the relative magnitudes of the different components of TKE remain fairly constant for weak stratification ($Fr_k > 2$), stratification effects begin to be experienced at increasing levels at different values of Fr_k for each of the simulation types. For the first and second types of forcing [Figs. 6(a1) and 6(b1)], there is an initial change at $Fr_k \approx 2$ and then again at $Fr_k \approx 0.3$. Moreover, for the first type of forcing, there is rapid growth in $\overline{uu}/2k$ with increasing stratification for $Fr_k < 0.3$, and for the second type of forcing, the magnitude of $\overline{uu}/2k$ surpasses that of $\overline{ww}/2k$ at $Fr_k = 0.3$ as well. For the third type of forcing, there is a change at $Fr_k \approx 0.7$, below which there is a rapid increase in $\overline{uu}/2k$ with increasing stratification.

Finally, we observe that the smallest component of the TKE for all three types of forcing is the one that is not associated with the nonzero Reynolds shear stress. For the first and second types of forcing [Figs. 6(a1) and 6(b1)], this is the spanwise component (squares), and for the third type of forcing [Fig. 6(c1)], this is the vertical component (triangles).

3. Reynolds shear stresses and turbulent buoyancy fluxes

We further quantify the turbulence anisotropy by considering the nonzero Reynolds shear stresses and turbulent buoyancy fluxes as a function of the turbulent Froude number for the three types of shear-forcing simulations [Figs. 6(a2)–6(c2)].

First, focusing on the Reynolds shear stresses (crosses) for the first and third types of forcing [Figs. 6(a2) and 6(c2)], the normalized Reynolds shear stresses are approximately constant (about -0.2) with increasing stratification until $Fr_k \approx 1$, and with further increasing stratification, they decrease towards zero for $Fr_k < 1$. For the second type of forcing [Fig. 6(b2)], the normalized

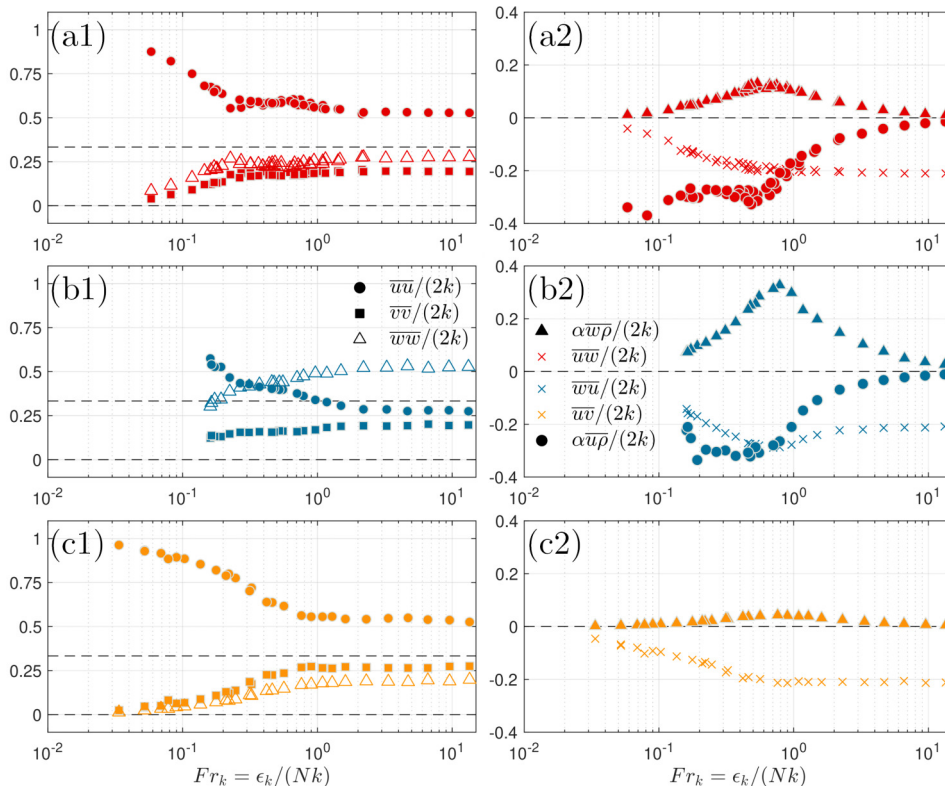


FIG. 6. Normalized mean-square streamwise (circles), spanwise (squares), and vertical (triangles) velocity fluctuations versus turbulent Froude number for the three forcing scenarios: (a1) type 1, (b1) type 2, and (c1) type 3. Also shown are the normalized values of the nonzero Reynolds shear stresses (colored crosses) and nonzero buoyancy flux vector components (triangles and circles) versus the turbulent Froude number for the three forcing scenarios: (a2) type 1, (b2) type 2, and (c2) type 3. In panels (a1)-(c1), the nonzero horizontal dashed line marks the value of $1/3$, which is expected of homogeneous isotropic turbulence.

Reynolds shear stress is also initially approximately constant (about -0.2), but unlike the other two types of forcing it increases in magnitude until $Fr_k \approx 0.7$. With further increasing stratification, however, the normalized Reynolds shear stress for this second type of forcing also begins to decrease towards zero.

Next we consider the normalized vertical buoyancy flux (closed triangles), which has been scaled to match the dimensions of TKE. Generally, for all three types of forcing, the normalized vertical buoyancy flux is negligible at weak stratification ($Fr_k \gg 1$) and it increases until reaching a peak around $Fr_k \approx 0.7$. With further increases in stratification, the normalized vertical buoyancy flux decreases towards zero. While there is this general agreement in the shape of the buoyancy flux curves, the three types of shear-forced, stably stratified turbulence exhibit very different peak magnitudes of the normalized vertical buoyancy fluxes: The second type [Fig. 6(b2)] exhibits the largest values and the third type [Fig. 6(c2)] exhibits the smallest values. This behavior is in agreement with the ordering of mixing efficiency B/P_k in Fig. 4. We explore this point further in later sections that discuss the energetics and mixing coefficient values for the three types of forcing.

Finally, for the first two types forcing [Figs. 6(a2) and 6(b2)], the streamwise buoyancy flux (closed circles) term is also significant. Broadly speaking, it is near zero for weak stratification ($Fr_k \gg 1$), but it increases and reaches a maximum at about the same Fr_k where the normalized

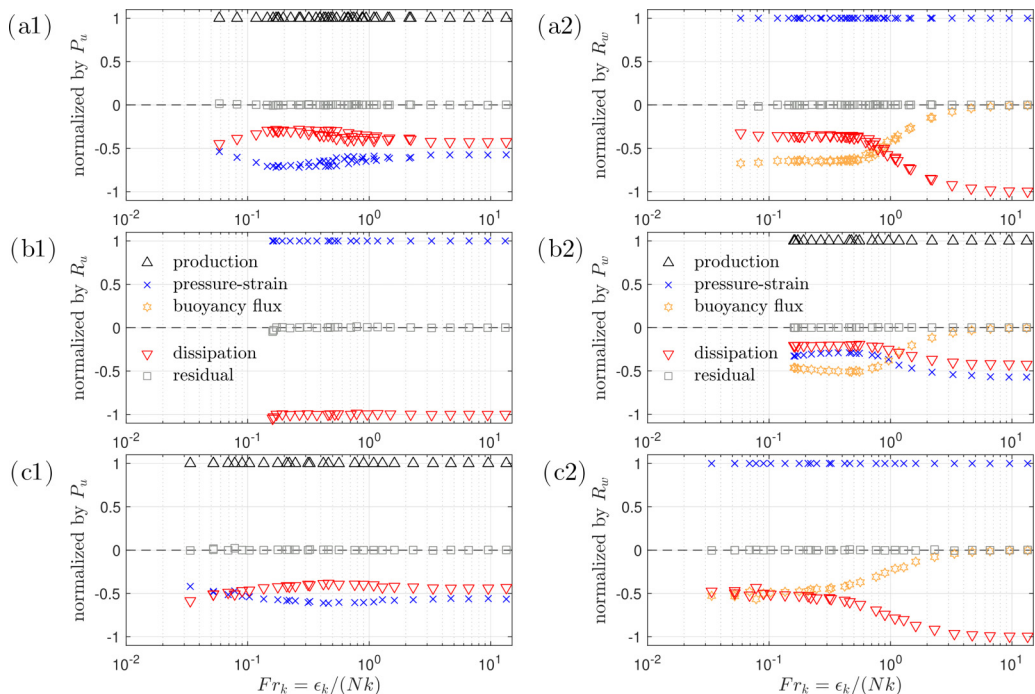


FIG. 7. Steady-state and volume- and time-averaged budgets of (a1)–(c1) $k_u = \overline{uu}/2$ [$i, j = 1$ in Eq. (7)] and (a2)–(c2) $k_w = \overline{ww}/2$ [$i, j = 3$ in Eq. (7)] as a function of the turbulent Froude number for the three types of forcing: (a) type 1, (b) type 2, and (c) type 3.

vertical buoyancy flux reaches its maximum ($Fr_k \approx 0.5$ compared to $Fr_k \approx 0.7$ for the vertical component). For the first type of forcing, the streamwise buoyancy flux seems to remain large and possibly even increases further for very strong stratifications ($Fr_k \approx 0.1$), but for the second type of forcing, the streamwise buoyancy flux begins to decrease for very strong stratifications ($Fr_k < 0.2$).

D. Normal Reynolds stress budgets

In this section we study the energetics of the three different types of shear-forced, stably stratified turbulence that bring about the turbulence anisotropy as presented in Sec. III C 2. This is the quantitative counterpart to the energy diagrams shown in Fig. 5. By decomposing the TKE into its three components [Eqs. (10)–(12)], we explicitly quantify the intercomponent exchange of TKE through the pressure-strain correlations and its relationship with the buoyancy flux to further quantify the differences among the three types of forcing. Here we normalize all terms in each budget by the sum of their respective production terms to keep all terms between ± 1 , and to match Eqs. (10)–(12) the normalized dissipation rates and the buoyancy flux are plotted with minus signs. Finally, we do not present the budgets of the spanwise component of TKE ($k_v = \overline{vv}/2$) since it is simply characterized by an exact balance between the pressure-strain correlations and rate of dissipation of k_v at all turbulent Froude numbers.

We first consider the budget of the streamwise component of TKE ($k_u = \overline{uu}/2$) for the three types of forcing [Figs. 7(a1)–7(c1)]. For the first and third types of forcing [Figs. 7(a1) and 7(c1)] we note that there is direct production of k_u (black triangles) and it is balanced by the pressure-strain correlation (blue crosses) and dissipation (red triangles) terms at all turbulent Froude numbers. For weak stratification ($Fr_k > 2$), the three terms maintain their relative importance. As stratification increases, the pressure-strain correlation becomes a stronger sink of k_u (especially for type 1) while

dissipation becomes a weaker sink of k_u . For strong stratification ($Fr_k < 0.2$ and $Fr_k < 0.3$ for the first and third types of forcing, respectively), however, the pressure-strain correlation becomes a weaker sink of k_u while dissipation becomes the stronger sink of k_u . For the first type of forcing, this continues until the two terms become almost equal at $Fr_k \approx 0.06$. For the third type of forcing, this also continues until the two terms become equal at $Fr_k \approx 0.07$, and for even stronger stratification we observe that dissipation becomes a larger sink of k_u compared to pressure-strain correlation. For the second type of forcing, k_u is indirectly generated by pressure-strain correlation and there is a balance between pressure-strain correlation and dissipation at all turbulent Froude numbers.

We next consider the budget of the vertical component of TKE ($k_w = \overline{w'w'}/2$) for the three types of forcing [Figs. 7(a2)–7(c2)]. For the first and third types of forcing [Figs. 7(a2) and 7(c2)] we note that k_w is indirectly generated by pressure-strain correlation (blue crosses) and this production is then balanced by buoyancy flux (orange stars) and dissipation (red triangles) at all turbulent Froude numbers. For weak stratification ($Fr_k > 2$), the buoyancy flux is negligible and the dominant balance is between the pressure-strain correlation and dissipation. As stratification increases, the buoyancy flux increases in magnitude and becomes a stronger sink of k_w while dissipation becomes a weaker sink of k_w . For the first type of forcing [Fig. 7(a2)], the buoyancy flux and dissipation become equal in magnitude at $Fr_k \approx 0.8$, and with further increases in stratification, the two terms remain relatively constant with the buoyancy flux as a slightly higher sink of k_w for $Fr_k < 0.5$. For the third type of forcing [Fig. 7(c2)], the buoyancy flux and dissipation become equal in magnitude at a stronger stratification ($Fr_k \approx 0.1$) compared to the first type of forcing, and for $Fr_k < 0.1$, the two sinks remain equally important sinks of k_w . Broadly speaking, the k_w budgets for the first and third types of forcing are similar (indirect generation by pressure strain and losses due to buoyancy flux and dissipation), but the first type of forcing is associated with the buoyancy flux playing a larger role as a sink of k_w [roughly 65%, with $B/R_w \approx -0.65$ for $Fr_k < 0.5$ in Fig. 7(a2)] compared to the third type of forcing [roughly 50%, with $B/R_w \approx -0.5$ for $Fr_k < 0.1$ in Fig. 7(c2)]. Alternatively, we can say that the first type of forcing is able to more efficiently convert k_w into TPE, which is why larger values of B/P_k are observed for the first type of forcing (red squares) compared to the third type of forcing (orange circles) in Fig. 4.

For the second type of forcing [Fig. 7(b2)], we note that, unlike for the two other forcing types, there is direct production of k_w (black triangles). As a result, the pressure-strain correlation is negative at all turbulent Froude numbers, indicating that k_w is being transformed into k_u rather than the other way around as with the first and third types of forcing. For weak stratification ($Fr_k > 2$), the buoyancy flux is negligible and k_w is generated by direct production (black triangles) and lost via pressure-strain correlation and dissipation with pressure-strain correlation being a larger sink of k_w relative to dissipation at all turbulent Froude numbers. As stratification increases, the buoyancy flux increases in magnitude, becoming equally important as dissipation at $Fr_k \approx 1.2$ and then equally important as pressure-strain correlation at $Fr_k \approx 1$. With further increases in stratification, the buoyancy flux becomes the most important sink of k_w and it (along with pressure-strain correlation and dissipation) remains relatively constant for $0.3 < Fr_k < 0.5$. For $Fr_k < 0.3$, the buoyancy flux begins to decrease in magnitude while the pressure-strain correlation increases in magnitude, implying that at these levels of stratification, converting k_w into k_u or k_v seems to be relatively easier than converting k_w into TPE. Returning to the observation that the second type of forcing (blue triangles) had the largest values of B/P_k , we note that this is likely due to the forcing directly generating k_w , which then can be transformed into TPE through the buoyancy flux. For the first and third types of forcing, the forcing directly generates k_u , some of which is then transformed into k_w through the pressure-strain correlation, which can then be transformed into TPE through the buoyancy flux. This additional step of converting k_u into k_w , which mathematically can be represented as $R_w/P_k < 1$, helps explain why, despite the magnitudes of B/R_w being large (0.65 and 0.5 in Figs. 7(a2) and 7(c2), respectively), the mixing efficiency values from the first and third types of forcing ($B/P_k = (B/R_w)(R_w/P_k)$) still end up being smaller compared to those from the

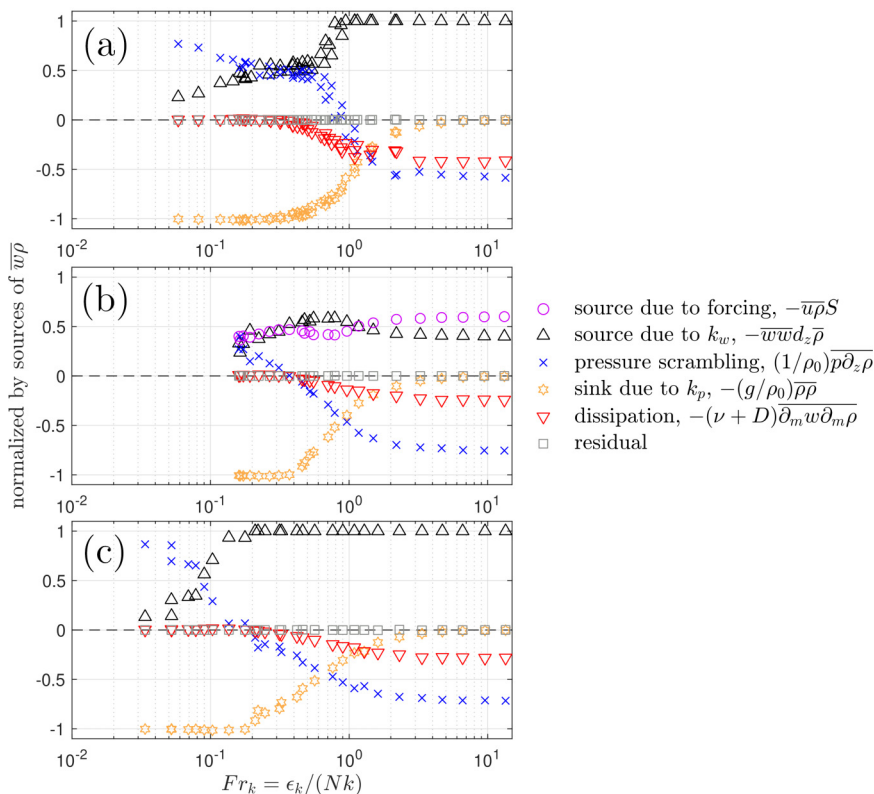


FIG. 8. Steady-state and volume- and time-averaged budgets of $\overline{w\rho}$ [Eq. (13)] as a function of the turbulent Froude number for the three types of forcing: (a) type 1, (b) type 2, and (c) type 3.

second type of forcing (see Fig. 4). We further explore this approach of rewriting B/P_k into its different components in Sec. III F.

E. Vertical buoyancy flux budget

We now consider the steady-state and volume- and time-averaged budgets of the vertical density flux $\overline{w\rho}$ [Eq. (13)] as a function of the turbulent Froude number for the three types of shear forcing in Figs. 8(a)–8(c). We note that the vertical density flux can be rewritten as the vertical buoyancy flux by multiplying by g/ρ_0 . We also normalize all terms in each budget by the sum of their respective production terms to keep all terms between ± 1 .

We first examine the vertical buoyancy flux budget for the first and third types of forcing [Figs. 8(a) and 8(c)]. For weak stratification ($Fr_k > 2$), the sink due to the k_p term (orange stars) is small and the dominant balance is between the source due to the k_w term (black triangles), pressure scrambling (blue crosses), and dissipation (red triangles). The pressure scrambling term is a larger sink for the third type of forcing compared to the first (about 71% of all sinks compared to about 57%). As stratification increases, the sink due to the k_p term increases in magnitude for both the first and third types of forcing until becoming the only significant sink of the vertical buoyancy flux at $Fr_k \approx 0.4$ and 0.2 , respectively. Analogously, the dissipation term decreases in magnitude until becoming negligible at $Fr_k \approx 0.4$ and 0.2 (for the first and third types of forcing) and the pressure scrambling term also exhibits important changes. For the first type of forcing, the pressure scrambling term switches sign at $Fr_k \approx 1$, thus becoming a source of vertical buoyancy flux, and it contributes equally as a source of vertical buoyancy flux with the source due to k_w term over the

range $0.2 < Fr_k < 0.5$. In contrast, for the third type of forcing, the pressure scrambling term only switches sign at stronger stratification ($Fr_k \approx 0.2$), and the pressure scrambling and source due to k_w term become equal in magnitude at $Fr_k \approx 0.08$. For $Fr_k < 0.08$, the pressure scrambling term becomes the dominant source of vertical buoyancy flux and the source due to the k_w term decreases in importance.

We next consider the vertical buoyancy flux budget for the second type of forcing [Fig. 8(b)]. Unlike the first and third types of forcing, there is an additional source term due to forcing (purple circles). For weak stratification ($Fr_k > 2$), the sink due to the k_p term (orange stars) is small and the dominant balance is between the source due to forcing (purple circles), the source due to k_w (black triangles), pressure scrambling (blue crosses), and dissipation (red triangles). As stratification increases, the sink due to the k_p term increases in magnitude until becoming the only significant sink of the vertical buoyancy flux at $Fr_k \approx 0.4$, and the dissipation term becomes negligible at $Fr_k \approx 0.4$ as well. This behavior is similar to what is observed for the first and third types of forcing. The pressure scrambling term, however, exhibits some notable differences compared to the first and third types of forcing. Because the first and second types of forcing connect the physics in the streamwise and vertical directions, we pay particular attention to the similarities and differences between these two cases. First, because there are two source terms for the vertical buoyancy flux for the second type of forcing, the pressure scrambling term has a delayed sign change (as the stratification increases) at $Fr_k \approx 0.4$ compared to the first type of forcing where it occurs at $Fr_k \approx 1$. Second, while the pressure scrambling term maintained an equal contribution to the source due to the k_w term for the first type of forcing, this behavior is not observed for the second type of forcing. This is because both the source due to forcing and the source due to k_w terms account for all generation of vertical buoyancy flux until $Fr_k \approx 0.4$. As the pressure scrambling term increases in magnitude and becomes a more important source of the vertical buoyancy flux, the other two source terms decrease in magnitude.

F. Mixing coefficient versus turbulent Froude number

Having considered the turbulence budgets in detail in the previous sections, we are now in a position to better understand the relationship between the mixing coefficient Γ and the turbulent Froude number Fr_k in Fig. 9(b). As noted earlier, for all stratification strengths (weak to strong), we observe an ordering of the values of Γ such that the second type of forcing (blue triangles) exhibits the largest values of Γ and the third type of forcing (orange circles) exhibits the smallest values of Γ . This indicates that the forcing mechanism (i.e., how the turbulence is generated) plays an important role in setting Γ . Broadly speaking, all three types of forcing exhibit the following relationship between Γ and Fr_k : (i) For weak stratification ($Fr_k > 1$), Γ increases with stratification; (ii) for moderate to strong stratification, Γ reaches a maximum value; and (iii) for very strong stratification, Γ begins to diminish from its peak value.

To connect some of these changes in the shape of how Γ varies with Fr_k , we plot the normalized pressure scrambling term as a function of Fr_k in Fig. 9(a) and the difference between the vertical component of TKE and TPE normalized by the total turbulent energy of the system as a function of Fr_k in Fig. 9(c). The normalized difference between k_w and k_p is meant to demonstrate the combined effect of the related source and sink terms that appear in the vertical buoyancy flux budget [cf. terms 3 and 4 on the RHS of Eq. (13), which can be reexpressed as $(k_w - k_p)N^2$ after multiplying through by g/ρ_0]. First, we note that for the first and second types of forcing (red squares and blue triangles), the normalized difference between k_w and k_p changes sign at $Fr_k \approx 0.8$ and 0.9 , respectively, whereas for the third type of forcing (orange circles), this occurs at $Fr_k \approx 0.2$. Connecting back to the budget of k_w in Figs. 7(a2)–7(c2), the Fr_k values associated with these sign changes correspond closely to when the buoyancy flux becomes a significant sink of k_w . With regard to the vertical buoyancy flux budget, this sign change implies that other terms in the budget need to adjust to keep $\overline{w\rho}$ positive for smaller values of Fr_k . For the first and third types of forcing, this is achieved with the sign change of the pressure scrambling term. However, for the second type of

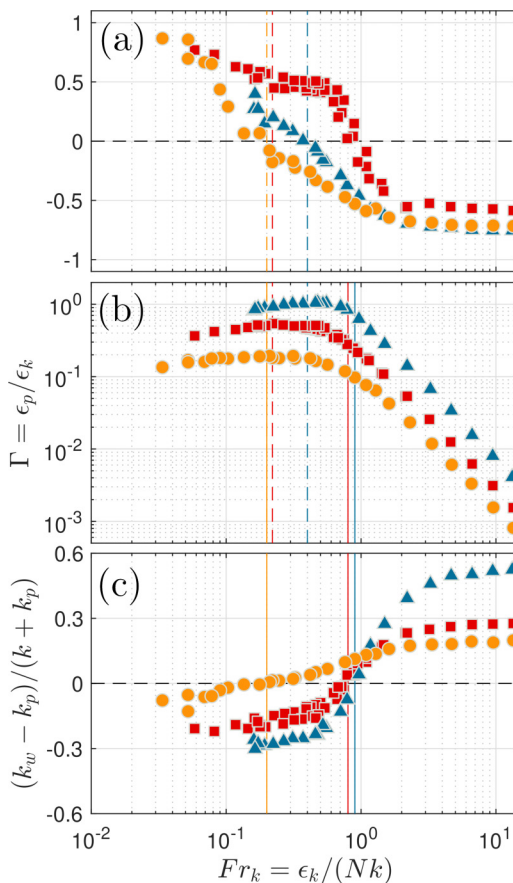


FIG. 9. Volume- and time-averaged values of (a) the normalized pressure scrambling term from the vertical buoyancy budget (see also Fig. 8), (b) the mixing coefficient Γ , and (c) the normalized difference between k_w and k_p as a function of the turbulent Froude number. The three color and symbol combinations correspond to the three forcing scenarios: type 1 (red squares), type 2 (blue triangle), and type 3 (orange circles).

forcing, the pressure scrambling term is still a sink of $\overline{w\rho}$ and the compensation is achieved by the additional source of $\overline{w\rho}$ due to forcing [purple circles in Fig. 8(b)].

Regarding how this connects to Γ , we note the following observations. First, for the first two types of forcing (red squares and blue triangles), the sign change of the normalized difference between k_w and k_p lines up closely with when Γ starts to plateau before reaching its maximum value ($Fr_k \approx 0.8$ and 0.9), whereas for the third type of forcing, this sign change lines up closely with the maximum value of Γ ($Fr_k \approx 0.2$). Second, for the second and third types of forcing (blue triangles and orange circles), the sign change of the pressure scrambling term lines up closely with the maximum value of Γ ($Fr_k \approx 0.4$ and 0.2), but for the first type of forcing (red triangles), the point where the pressure scrambling term increases beyond 0.5 seems to be a better indicator of the maximum value of Γ ($Fr_k \approx 0.2$). Further increases in the pressure scrambling term are associated with less efficient mixing, indicated by $\Gamma < \Gamma_{\max}$, which has also been observed for axisymmetric stratified turbulence [40]. One interpretation of this might be that as the buoyancy flux is increasingly generated by the pressure scrambling mechanism, the conversion of k_w to k_p becomes less effective [B becomes less efficient in Figs. 5(a) and 5(b)]. Interestingly, for the second type of forcing, which involves direct generation of k_w , we observe that k_u becomes the largest component of TKE for $Fr_k < 0.3$, indicating that the conversion of k_w to k_u becomes more favorable relative to the

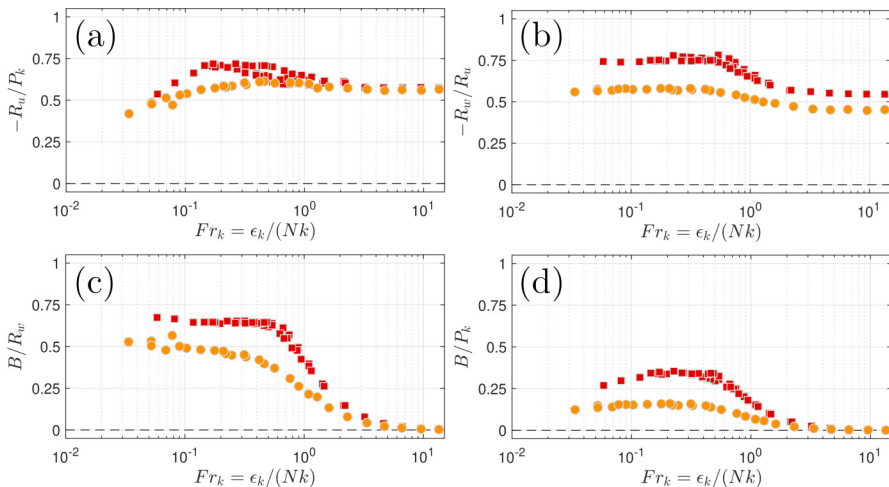


FIG. 10. Terms on the RHS of Eq. (14) and the mixing efficiency B/P_k as a function of Fr_k for the first and third types of forcing (red squares and orange circles).

conversion of k_w to k_p [R_u becomes more efficient than B in Fig. 5(b)]. In Fig. 7(b2) we see this trade-off between the pressure-strain correlation (blue crosses) and the buoyancy flux (orange stars) as sinks of k_w .

Before closing this section, we also quantitatively explore the role that direct versus indirect generation of k_w plays for Γ . Recall that for the first and third types of forcing, k_u is directly generated. Some of this gets converted to k_w through the pressure-strain correlation term before finally getting converted to k_p through the buoyancy flux. Therefore, k_p is generated in two steps. For the second type of forcing, however, k_w is directly generated and therefore the buoyancy flux can directly convert some of this energy to k_p , making this a single-step process. To quantitatively consider this effect, we rewrite the irreversible mixing efficiency for the first and third types of forcing as follows:

$$Ri_f = \frac{B}{P_k} = \left(-\frac{R_u}{P_k} \right) \left(-\frac{R_w}{R_u} \right) \left(\frac{B}{R_w} \right). \quad (14)$$

The first term ($-R_u/P_k$) represents how much of the TKE generation gets used to generate k_v and k_w . For incompressible flow, the continuity equation dictates $R_u + R_v + R_w = 0$, but here we are particularly interested in how much of R_u goes to generating k_w , which is represented by the second term ($-R_w/R_u$). Finally, the third term (B/R_w) represents how much of this indirect generation of k_w gets used to generate k_p . Therefore, for the first and third types of forcing, the overall mixing efficiency B/P_k is set by the individual efficiencies of the three terms on the RHS of Eq. (14).

In Fig. 10 we explore the three terms on the RHS of Eq. (14) as a function of Fr_k for the first and third types of forcing (red squares and orange circles). We first consider $-R_u/P_k$ as a function of Fr_k in Fig. 10(a). For weak stratification, both types of forcing have similar values between 0.56 and 0.58. As stratification increases ($Fr_k < 1$), however, we begin to observe deviations such that the first type of forcing (red squares) exhibits more of the TKE generation being available to indirectly generate k_v and k_w compared to the third type of forcing (orange squares). For both types of forcing, we see that this indirect generation mechanism becomes less efficient at very strong stratifications ($Fr_k < 0.2$). For the first type of forcing, the scatter in $0.3 < Fr_k < 0.7$ is due to Reynolds-number variations at fixed Fr_k , which is explored in Ref. [41].

We next consider $-R_w/R_u$ as a function of Fr_k in Fig. 10(b). For all stratification strengths, we see that the first type of forcing (red squares) is able to use more of $-R_u$ for generating k_w

compared to the third type of forcing (orange circles). For weak stratification, about 55% of $-R_u$ is used to generate k_w for the first type of forcing, whereas about 45% of $-R_u$ is used to generate k_w for the third type of forcing. As stratification increases ($\text{Fr}_k < 1$), both types of forcing exhibit an increase of $-R_w/R_u$ before reaching a plateau of about 75% and 57%, respectively, around $\text{Fr}_k \approx 0.5$, which is maintained for even stronger stratifications. We note that unlike in Fig. 10(a), the Reynolds-number effects seem to be minimal for this particular ratio of terms as noted by the reduced scatter of the red squares for $0.3 < \text{Fr}_k < 0.7$.

We finally consider B/R_w as a function of Fr_k in Fig. 10(c). For weak stratification, this term is near zero, indicating very weak coupling between k_w and k_p , but as stratification increases ($\text{Fr}_k < 3$), we observe that the first type of forcing is always more effective in using R_w for generating k_p through B . The first type of forcing exhibits a plateau of $B/R_w \approx 0.65$, which first occurs at $\text{Fr}_k \approx 0.5$, whereas the third type of forcing exhibits a plateau of $B/R_w \approx 0.5$, which first occurs at $\text{Fr}_k \approx 0.2$.

Combining these three terms together, we take a final look at $\text{Ri}_f = B/P_k$ as a function of Fr_k in Fig. 10(d). Given that the second and third terms both exhibit plateaus for strong stratification, the reduced mixing efficiency for $\text{Fr}_k < 0.2$ for both types of forcing can only be explained by the reduced efficiency of $-R_u/P_k$ at strong stratifications. Also, the more efficient mixing associated with the first type of forcing compared to the third type of forcing is the result of all three conversion steps [i.e., three terms on the RHS of Eq. (14)] being more efficient.

G. Alternative expression for the mixing efficiency and comments on Reynolds-number effects

Until now, we have presented our results mostly in terms of Fr_k [and implicitly in terms of Ri_g and S_* given they are related to Fr_k as shown in Fig. 3(b)]. Our simulations, however, also exhibit Reynolds number variations (e.g., Re_L , Re_b , and Re_S). While the primary variations of our quantities of interest have been captured by Fr_k , we expect our results to change when the Reynolds number is increased, albeit to a lesser degree than the variations demonstrated as a function of Fr_k [34,35].

Following Ref. [44], we can express the mixing efficiency Ri_f in an alternative way as

$$\text{Ri}_f = \frac{1}{1 - c_3} \left(\frac{R_w}{P_k} - c_3 \right), \quad (15a)$$

$$\text{Ri}_f = \frac{1}{1 - c_3} \left(1 + \frac{R_w}{P_k} - c_3 \right), \quad (15b)$$

where R_w/P_k is the pressure-strain correlation term from the k_w budget normalized by the TKE production and $c_3 = \epsilon_w/\epsilon_k$ is the ratio of the dissipation rate of k_w to the TKE dissipation rate. Equation (15a) applies to the first and third types of forcing and Eq. (15b) applies second type of forcing, where the additional term arises from the shear forcing term in the k_w budget. To arrive at Eqs. (15a) and (15b), we take the k_w budget, divide by the TKE production term P_k , and using the total energy balance at steady state (i.e., $P_k = \epsilon_k + \epsilon_p$ and $B = \epsilon_p$) isolate Ri_f .

Taking the limit as $\text{Re} \gg 1$, where we expect $c_3 \rightarrow 1/3$ from local isotropy, the two expressions can be rewritten as

$$\lim_{\text{Re} \gg 1} \text{Ri}_f = \frac{3}{2} \left(\frac{R_w}{P_k} \right) - \frac{1}{2}, \quad (16a)$$

$$\lim_{\text{Re} \gg 1} \text{Ri}_f = 1 + \frac{3}{2} \left(\frac{R_w}{P_k} \right). \quad (16b)$$

While there are three candidates for Re (Re_S , Re_b , and Re_L), here we choose the Reynolds number that best represents the range of isotropic scales of motion. Given that $S_* > 1$ is typically observed for unstratified and stratified turbulent shear flows [81,82], $\text{Re} = \text{Re}_S$ for $\text{Ri}_g \leq 1$ and $\text{Re} = \text{Re}_b$ for $\text{Ri}_g \geq 1$ [83]. This is because for $\text{Ri}_g < 1$, the Corrsin scale is smaller than the Ozmidov scale, while for $\text{Ri}_g > 1$, the Ozmidov scale is smaller than the Corrsin scale. For $\text{Ri}_g = 1$, the two scales

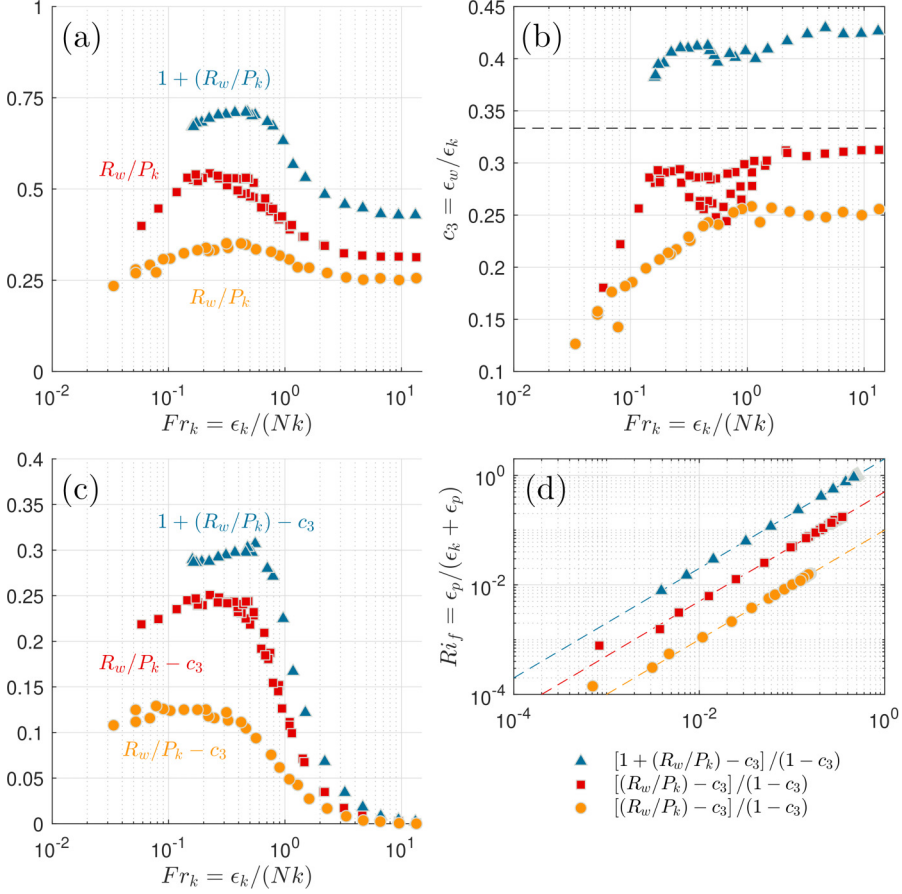


FIG. 11. Plots of (a) R_w/P_k (types 1 and 3) and $1 + R_w/P_k$ (type 2), (b) $c_3 = \epsilon_w/\epsilon_k$, (c) $R_w/P_k - c_3$ (types 1 and 3) and $1 + (R_w/P_k) - c_3$ (type 2) as a function of Fr_k . (d) Plot of Ri_f as a function of the terms on the RHSs of Eqs. (15).

are equivalent. Recalling the energy exchange diagrams in Fig. 5 (and also that all three systems considered here involve a net downscale transfer of energy), Eqs. (16) demonstrate that the eventual ratio of the TPE and TKE dissipation rates is determined at larger scales of motion that contribute most to R_w and P_k .

Using the volume- and time-averaged statistics from our three sets of simulations, we evaluate the RHSs of Eqs. (15a) and (15b) in Fig. 11. First, in Fig. 11(a) we plot the terms in the parentheses that are not c_3 as a function of Fr_k , which broadly represent the large-scale contributions to Ri_f . We note that the three sets of simulations are ordered as before with the second type of forcing (blue triangles) having the largest values and the third type of forcing (orange circles) having the smallest values. Next, in Fig. 11(b) we plot the ratio of the dissipation rates of k_w and k as a function of Fr_k for the three types of forcing. The horizontal dashed line indicates $1/3$, which is expected for $Re \gg 1$. Once again, we see the same ordering in the magnitudes of c_3 across the three types of forcing, and the scatter for $0.3 < Fr_k < 1$ is due to Reynolds-number effects, which is studied in Ref. [41]. While our data sets do not exhibit $c_3 \rightarrow 1/3$ even for the weakly stratified conditions ($Fr_k > 1$) (especially the second and third types of forcing in blue stars and orange circles), this is likely because our simulations are characterized by $Re_S < 50$ (see Tables III–V), which is substantially below the high-Re limit. For homogeneous, stably stratified, vertically sheared turbulence, small-scale anisotropy has been shown to decrease with increasing Re [35,84], but it persists even

up to $Re_S \approx 140$ for $Ri_g \approx 0.15$ (see Fig. 2 of [35]). Then, in Fig. 11(c) we plot the combined effects of the parenthetical terms as a function of Fr_k . The same ordering remains after taking the difference of the terms in Figs. 11(a) and 11(b) with the values for weak stratification approaching 0. As a final check, we plot Ri_f as a function of the terms on the RHSs of Eqs. (15a) and (15b). Apart from the two most weakly stratified simulations for the first and third types of forcing, all simulations lie close to their respective one-to-one lines (offset by factors of 2, 0.5, and 0.1), indicating that the flow statistics are representative of statistically stationary conditions.

IV. CONCLUSION

In this work we studied three different types of shear-forced, stably stratified turbulence under statistically stationary conditions. Given that the three types of shear forcing interacted differently with the background vertical stratification (Figs. 2 and 5), we sought to understand how their distinct large-scale anisotropy would affect their mixing characteristics. We found a number of notable results. First, as we increased stratification, the component of TKE that was directly generated increased monotonically except for the second type of forcing where the streamwise component overtook the vertical component of TKE at $Fr_k \approx 0.3$ [Fig. 6(b1)]. Second, we quantified the streamwise and vertical Reynolds stress budgets as a function of Fr_k (Fig. 7), highlighting the importance of the pressure-strain correlation terms in generating k_w for the first and third types of forcing, where only k_u is directly generated by the shear forcing. For the second type of forcing, where k_w is directly generated, this led to negative values of the pressure-strain correlation term at all values of Fr_k . Third, we quantified the vertical buoyancy flux budgets as a function of Fr_k (Fig. 8), where with increasing stratification we observed the sign change of the pressure scrambling term, making it a source of $\overline{w\rho}$, which was accompanied by a decrease in the magnitudes of the dissipation and the source due to k_w and source due to forcing terms. For strong stratification, the sink due to k_p always became the sole sink of $\overline{w\rho}$. Fourth, we considered the mixing coefficient Γ as a function of Fr_k . We observed a persistent ordering in the values of Γ from weak to strong stratification (spanning two orders of magnitude of Fr_k), which indicates that the turbulence generation mechanism and the resulting transfer of energy among the components of TKE and TPE have a significant effect on the mixing properties of stratified turbulence. In particular, we observed important changes in Γ when the normalized difference $(k_w - k_p)/(k + k_p)$ changed signs as well as when the pressure scrambling term either changed signs (for the second and third types of forcing) or significantly deviated from a fixed value that had persisted over a range of Fr_k (for the first type of forcing). Fifth, drawing on the energy exchange diagrams (Fig. 5) and the fact that the first and third types of shear forcing involve indirect generation of k_w , we decomposed the mixing efficiency into three separate energy conversion steps and quantified the efficiency of each of these steps (Fig. 10). We found that the Γ values associated with the first type of forcing being larger than those associated with the third type of forcing is due to all three conversion steps being more efficient for the first type of forcing. Finally, we considered alternative expressions for the mixing efficiency (Fig. 11). Taking the limit of large Reynolds number, the expressions simplified such that the mixing efficiency was solely set by the ratio of the pressure-strain term from the k_w budget and the TKE production (R_w/P_k). This indicates that while Reynolds-number effects are present for finite Reynolds numbers, given the net downscale energy transfer associated with these systems, the mixing efficiency is primarily determined at the large scales, namely, based on how much of the TKE production can be used for intercomponent exchange through R_w .

Given that our analyses have shown the important relationship between the mixing coefficient Γ and the pressure-strain correlations and pressure scrambling terms, there is a need to develop a more robust physical understanding of these terms. In particular, for Reynolds-averaged Navier-Stokes simulations, models for the pressure scrambling term remain a major source of uncertainty for estimating turbulent passive scalar fluxes and therefore the mean passive scalar concentration field (see, e.g., Ref. [77]). For stratified flows, this challenge becomes even more significant given that the Reynolds stresses and turbulent buoyancy fluxes are coupled so that errors in either can affect

the predictions of the mean momentum and buoyancy fields. Following some previous works in the geophysical context (e.g., Refs. [85–88]), the pressure-strain and pressure scrambling terms from our DNS data sets could be further analyzed by decomposing the pressure fluctuations into one slow and two rapid components, where the one slow pressure component is associated with nonlinear effects and the two rapid pressure components are associated with the shear forcing and buoyancy effects. In particular, it will be interesting to see how these three pressure components contribute to the observed sign changes for the total pressure scrambling term [Fig. 9(a)]. Furthermore, existing Reynolds stress and scalar flux models that have been applied to various stratified turbulent flows (e.g., Refs. [89–91]) could be applied to our three DNS data sets to test the validity of their modeling assumptions for the pressure-strain and pressure scrambling terms, especially in the limit of very strong stratification.

Regarding the accurate representation of irreversible mixing in large-scale ocean simulations, our results indicate that knowing how the turbulence is generated is of leading order importance in determining the value of Γ , which is needed to estimate the turbulent diffusivity D_T for the density field. This means that rather than seeking a universal description of Γ as a function of Re_b or Fr_k (see, e.g., [18,36]), more sophisticated approaches for estimating Γ are necessary. With regard to ocean measurements, our results suggest that one needs to know what type of turbulence generation mechanism the measured values of ϵ_k are associated with in order to appropriately determine Γ . A likely approach for moving forward might involve using a classification algorithm as in Ref. [92] to determine what type of turbulence generation mechanism is active and apply specific fits for Γ in terms of turbulence parameters such as Fr_k and S_* (see, e.g., Ref. [41]) or an equivalent description based on length-scale ratios (see, e.g., Ref. [93]).

ACKNOWLEDGMENTS

Y.R.Y. gratefully acknowledges support from the Charles H. Leavell Fellowship of the Department of Civil and Environmental Engineering at Stanford University. Most of the computing for this project was performed on the Sherlock cluster. We would like to thank Stanford University and the Stanford Research Computing Center for providing computational resources and support that contributed to these research results.

APPENDIX A: REYNOLDS SHEAR STRESS AND STREAMWISE BUOYANCY FLUX BUDGETS

Here we consider the budget for the nonzero Reynolds shear stress component for the three forcing scenarios. For the first two types of forcing, the nonzero component is \overline{uw} , and for the third type of forcing, the nonzero component is \overline{wv} . All terms have been normalized so that they are between ± 1 , and since the Reynolds shear stresses are negative, their source terms will occupy the negative halves of the y axes.

We first consider the budget for \overline{uw} for the first two types of forcing in Figs. 12(a) and 12(b). For both types of forcing, the sink due to the $\overline{u\rho}$ term (orange stars) is small for weak stratification and there is a balance between three terms: source due to k_w and k_u [for the first and second types of forcing, respectively (black triangles)], pressure strain (blue crosses), and dissipation (red triangles). As stratification increases, the sink due to the $\overline{u\rho}$ term becomes more important and this change is accompanied by the pressure-strain and dissipation terms becoming less important sinks of \overline{uw} . For the first type of forcing, the pressure strain and sink due to the $\overline{u\rho}$ terms become equally important at $Fr_k \approx 0.8$, while for the second type of forcing, the two terms become equally important at $Fr_k \approx 0.5$. With stronger stratification ($Fr_k < 0.8$), for the first type of forcing, we observe that the pressure-strain correlations change signs at $Fr_k \approx 0.3$, becoming a source of \overline{uw} , and it becomes equally important as the source due to k_w at $Fr_k \approx 0.11$ and even eclipses it to become the most important source of \overline{uw} for $Fr_k < 0.11$. With stronger stratification ($Fr_k < 0.5$), for the second type of forcing, the sink due to the $\overline{u\rho}$ term becomes the most important loss term of \overline{uw} , but for the simulations with strongest stratification, the pressure-strain term seems to grow

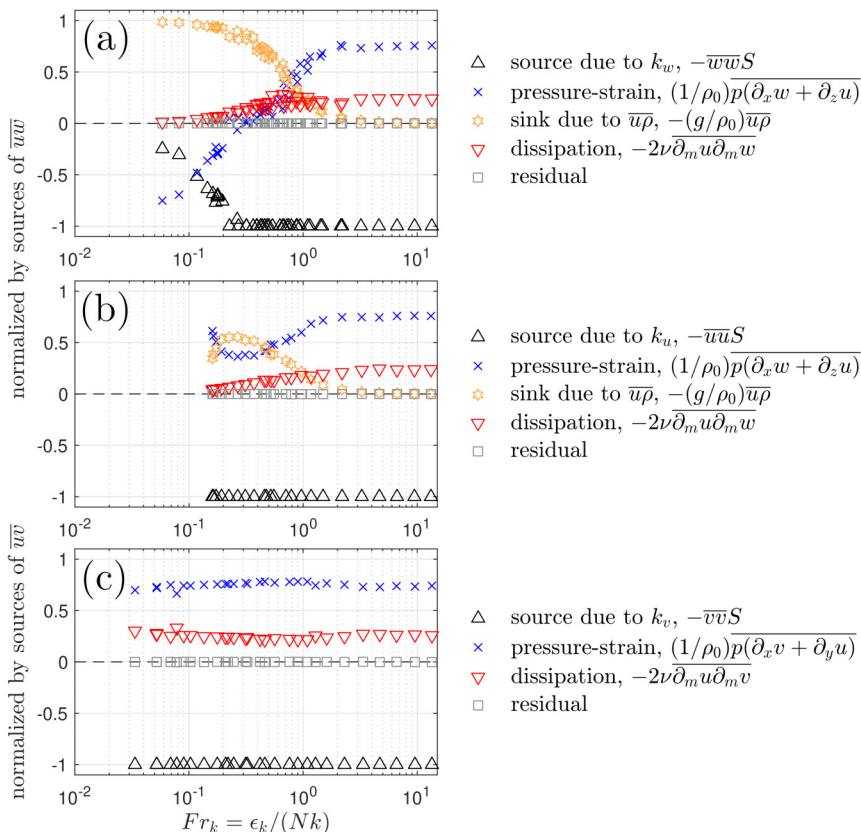


FIG. 12. Steady-state and volume- and time-averaged budgets of the nonzero Reynolds shear stresses [nonzero $i \neq j$ components of Eq. (7)] as a function of the turbulent Froude number for the three types of forcing: (a) type 1, (b) type 2, and (c) type 3.

in importance once more, eclipsing the sink due to $\overline{u\rho}$. This behavior, however, needs to be studied with larger simulations that would allow one to explore $Fr_k < 0.1$ at higher Reynolds numbers.

We next consider the budget for \overline{uv} for the third type of forcing in Fig. 12(c). We note that this particular shear stress component does not involve w , which is the direction where the buoyancy force is directly active. Interestingly (because of this fact), we find that for all stratification strengths (across two orders of magnitude of Fr_k), the relative importance of the terms in the \overline{uv} budget remains largely unchanged. The source term due to k_v is the only generation mechanism for \overline{uv} , and the dissipation and pressure-strain terms are the two sinks of \overline{uv} with the pressure-strain term being more significant.

Now we consider the budgets of the streamwise component of the density flux vector ($\overline{u\rho}$) in Figs. 13(a) and 13(b). All terms have been normalized so that they are between ± 1 , and since the streamwise buoyancy flux is negative, its source terms will occupy the negative half of the y axis.

For the first type of shear forcing [Fig. 13(a)], there are two source terms of $\overline{u\rho}$, which are the sources due to $\overline{w\rho}$ and \overline{uw} (black circles and black triangles, respectively), and two sink terms of $\overline{u\rho}$, which are the dissipation (red triangles) and pressure scrambling (blue crosses) terms. As stratification is increased, the first notable change occurs at $Fr_k \approx 1$, where the dissipation term decreases and the pressure scrambling increases. The next notable change occurs at $Fr_k \approx 0.4$, where the two sources of $\overline{u\rho}$ become equally important; as stratification is increased further ($Fr_k < 0.4$), the source due to \overline{uw} becomes the more important source of $\overline{u\rho}$. Interestingly, the dissipation term

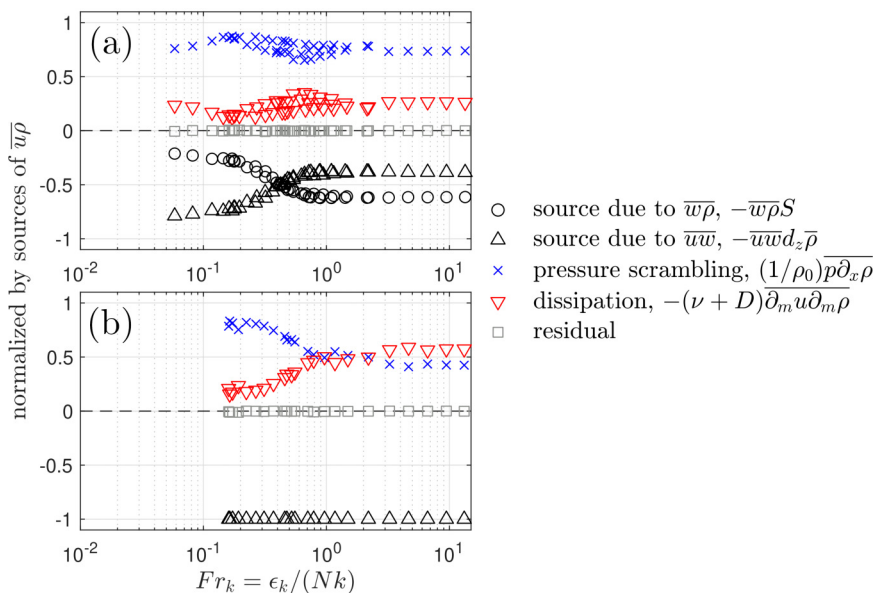


FIG. 13. Steady-state and volume- and time-averaged budgets of $\overline{u\rho}$ [the $j = 1$ component of Eq. (8)] as a function of the turbulent Froude number for the (a) first and (b) second types of forcing.

begins to increase in magnitude for $Fr_k < 0.1$, which is accompanied by a decrease in magnitude of the pressure scrambling term, which is in contrast to the dissipation term approaching zero for strong stratification in the Reynolds shear stress and vertical density flux budgets.

For the second type of shear forcing [Fig. 13(b)], there is only one source term for $\overline{u\rho}$, which is the source due to \overline{uw} (black triangles), and there are two sink terms of $\overline{u\rho}$, which are the pressure scrambling (blue crosses) and dissipation (red triangles) terms. As stratification is increased, the first notable change occurs at $Fr_k \approx 1$, where the pressure scrambling and dissipation terms are equally important sinks of $\overline{u\rho}$. As stratification is further increased ($Fr_k < 1$), the pressure scrambling term becomes increasingly important as a sink of $\overline{u\rho}$ while the dissipation becomes less important.

APPENDIX B: TURBULENT PRANDTL NUMBER VERSUS TURBULENT FROUDE NUMBER

Here we consider the turbulent Prandtl number $Pr_T = \nu_T/D_T$ for the three shear forcing scenarios, which is defined as

$$Pr_T = \frac{-\overline{uw}}{\alpha \overline{w\rho}} Ri_g^{1/2}, \quad (\text{B1a})$$

$$Pr_T = \frac{-\overline{uw}}{\alpha \overline{w\rho}} Ri_g^{1/2}, \quad (\text{B1b})$$

with Eq. (B1a) for the first two forcing types and Eq. (B1b) for the third forcing type. The turbulent Prandtl number is often used to algebraically estimate the turbulent scalar diffusivity with a known model for the turbulent viscosity ν_T . For stratified flows, Pr_T is known to vary strongly with stratification (see, e.g., Fig. 1 of Ref. [94]).

In Fig. 14(a) we plot the normalized Reynolds shear stresses as a function of Fr_k . For weak stratification ($Fr_k > 3$), the normalized Reynolds shear stresses have a value of 0.2. For the first and third forcing types (red and orange, respectively), the normalized Reynolds shear stresses decrease monotonically with Fr_k . For the second forcing type (blue), however, the normalized Reynolds shear stress reaches a maximum at $Fr_k \approx 0.7$ before decreasing with Fr_k .

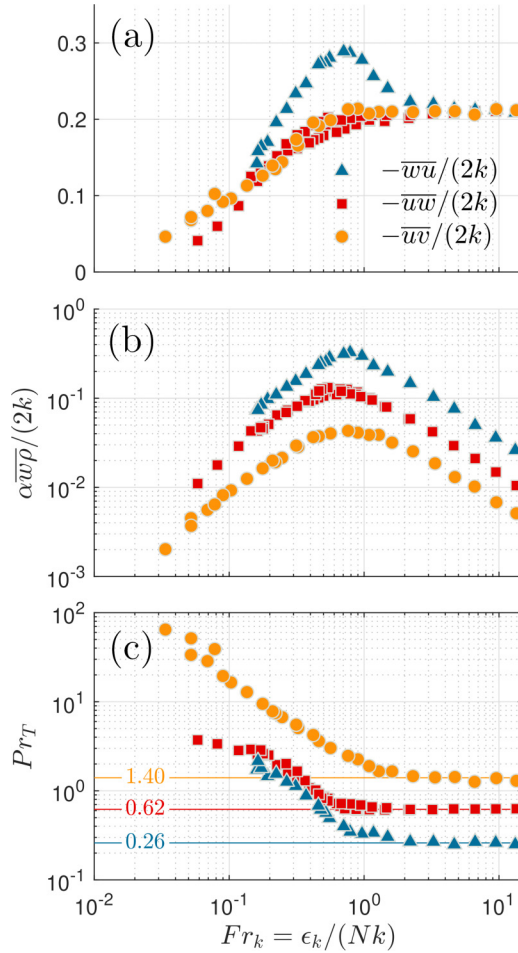


FIG. 14. Steady-state and volume- and time-averaged values of the (a) normalized Reynolds shear stresses, (b) normalized vertical buoyancy flux, and (c) turbulent Prandtl number as a function of Fr_k .

Next we plot the normalized vertical buoyancy flux as a function of Fr_k [Fig. 14(b)]. At all values of Fr_k , the values of the vertical buoyancy flux are ordered such that those from the second forcing type (blue) are largest and those from the third forcing type (orange) are smallest. The normalized vertical buoyancy flux has a maximum at $Fr_k \approx 0.7$.

Finally, we plot the turbulent Prandtl number as a function of Fr_k [Fig. 14(c)]. For weak stratification ($Fr_k > 3$), the three types of forcing exhibit relatively constant values of $Pr_T \approx 0.62$, 0.26, and 1.40, respectively. With increasing stratification, we observe that Pr_T increases monotonically for $Fr_k < 1$. Given that both the numerator and denominator of Pr_T are broadly decreasing for $Fr_k < 1$ (apart from the initial increase in \overline{wu} for the second type of forcing), the increase in Pr_T indicates that the vertical buoyancy flux is decreasing faster with decreasing Fr_k than the Reynolds shear stress.

-
- [1] C. Wunsch and R. Ferrari, Vertical mixing, energy, and the general circulation of the oceans, *Annu. Rev. Fluid Mech.* **36**, 281 (2004).
 [2] J. R. Taylor and A. F. Thompson, Submesoscale dynamics in the upper ocean, *Annu. Rev. Fluid Mech.* **55**, 103 (2023).

-
- [3] A. Adcroft, W. Anderson, V. Balaji, C. Blanton, M. Bushuk, C. O. Dufour, J. P. Dunne, S. M. Griffies, R. Hallberg, M. J. Harrison, I. M. Held, M. F. Jansen, J. G. John, J. P. Krasting, A. R. Langenhorst, S. Legg, Z. Liang, C. McHugh, A. Radhakrishnan, B. G. Reichl *et al.*, The GFDL global ocean and sea ice model OM4.0: Model description and simulation features, *J. Adv. Model. Earth Syst.* **11**, 3167 (2019).
- [4] B. Fox-Kemper, A. Adcroft, C. W. Böning, E. P. Chassignet, E. Curchitser, G. Danabasoglu, C. Eden, M. H. England, R. Gerdes, R. J. Greatbatch, S. M. Griffies, R. W. Hallberg, E. Hanert, P. Heimbach, H. T. Hewitt, C. N. Hill, Y. Komuro, S. Legg, J. Le Sommer, S. Masina *et al.*, Challenges and prospects in ocean circulation models, *Front. Mar. Sci.* **6**, 65 (2019).
- [5] F. Bryan, Parameter sensitivity of primitive equation ocean general circulation models, *J. Phys. Oceanogr.* **17**, 970 (1987).
- [6] S. R. Jayne, The impact of abyssal mixing parameterizations in an ocean general circulation model, *J. Phys. Oceanogr.* **39**, 1756 (2009).
- [7] C. de Lavergne, G. Madec, J. Le Sommer, A. J. G. Nurser, and A. C. Naveira Garabato, The impact of a variable mixing efficiency on the abyssal overturning, *J. Phys. Oceanogr.* **46**, 663 (2016).
- [8] A. Mashayek, H. Salehipour, D. Bouffard, C. P. Caulfield, R. Ferrari, M. Nikurashin, W. R. Peltier, and W. D. Smyth, Efficiency of turbulent mixing in the abyssal ocean circulation, *Geophys. Res. Lett.* **44**, 6296 (2017).
- [9] L. Cimoli, C. P. Caulfield, H. L. Johnson, D. P. Marshall, A. Mashayek, A. C. Naveira Garabato, and C. Vic, Sensitivity of deep ocean mixing to local internal tide breaking and mixing efficiency, *Geophys. Res. Lett.* **46**, 14622 (2019).
- [10] T. R. Osborn, Estimates of the local rate of vertical diffusion from dissipation measurements, *J. Phys. Oceanogr.* **10**, 83 (1980).
- [11] H. Salehipour and W. R. Peltier, Diapycnal diffusivity, turbulent Prandtl number and mixing efficiency in Boussinesq stratified turbulence, *J. Fluid Mech.* **775**, 464 (2015).
- [12] S. K. Venayagamoorthy and J. R. Koseff, On the flux Richardson number in stably stratified turbulence, *J. Fluid Mech.* **798**, R1 (2016).
- [13] G. N. Ivey and J. Imberger, On the nature of turbulence in a stratified fluid. Part I: The energetics of mixing, *J. Phys. Oceanogr.* **21**, 650 (1991).
- [14] G. N. Ivey, K. B. Winters, and J. R. Koseff, Density stratification, turbulence, but how much mixing? *Annu. Rev. Fluid Mech.* **40**, 169 (2008).
- [15] M. C. Gregg, E. A. D'Asaro, J. J. Riley, and E. Kunze, Mixing efficiency in the ocean, *Annu. Rev. Mar. Sci.* **10**, 443 (2018).
- [16] C. P. Caulfield, Open questions in turbulent stratified mixing: Do we even know what we do not know? *Phys. Rev. Fluids* **5**, 110518 (2020).
- [17] C. P. Caulfield, Layering, instabilities, and mixing in turbulent stratified flows, *Annu. Rev. Fluid Mech.* **53**, 113 (2021).
- [18] S. G. Monismith, J. R. Koseff, and B. L. White, Mixing efficiency in the presence of stratification: When is it constant?, *Geophys. Res. Lett.* **45**, 5627 (2018).
- [19] <https://microstructure.ucsd.edu>.
- [20] K. A. Davis and S. G. Monismith, The modification of bottom boundary layer turbulence and mixing by internal waves shoaling on a barrier Reef, *J. Phys. Ocean.* **41**, 2223 (2011).
- [21] R. K. Walter, M. E. Squibb, C. B. Woodson, J. R. Koseff, and S. G. Monismith, Stratified turbulence in the nearshore coastal ocean: Dynamics and evolution in the presence of internal bores, *J. Geophys. Res.: Ocean.* **119**, 8709 (2014).
- [22] J. F. Dunckley, Mixing in nearshore coastal environments, Ph.D. thesis, Department of Civil and Environmental Engineering, Stanford University, 2012, <https://searchworks.stanford.edu/view/9698536>.
- [23] M. E. Squibb, Dynamics of shoaling internal waves in the near-shore: Mamala Bay, Hawaii, Ph.D. thesis, Department of Civil and Environmental Engineering, Stanford University, 2014, <https://searchworks.stanford.edu/view/10701346>.
- [24] R. C. Holleman, W. R. Geyer, and D. K. Ralston, Stratified turbulence and mixing efficiency in a salt wedge, *J. Phys. Oceanogr.* **46**, 1769 (2016).

- [25] J. Rohr and C. van Atta, Mixing efficiency in stably stratified growing turbulence, *J. Geophys. Res.* **92**, 5481 (1987).
- [26] L. H. Shih, J. R. Koseff, G. N. Ivey, and J. H. Ferziger, Parameterization of turbulent fluxes and scales using homogenous sheared stably stratified turbulence simulations, *J. Fluid Mech.* **525**, 193 (2005).
- [27] D. Chung and G. Matheou, Direct numerical simulation of stationary homogeneous stratified sheared turbulence, *J. Fluid Mech.* **696**, 434 (2012).
- [28] Q. Zhou, J. R. Taylor, and C. P. Caulfield, Self-similar mixing in stratified plane Couette flow for varying Prandtl number, *J. Fluid Mech.* **820**, 86 (2017).
- [29] G. Brethouwer, P. Billant, and J. M. Chomaz, Scaling analysis and simulation of strongly stratified turbulent flows, *J. Fluid Mech.* **585**, 343 (2007).
- [30] R. S. Arthur, S. K. Venayagamoorthy, J. R. Koseff, and O. B. Fringer, How we compute N matters to estimates of mixing in stratified flows, *J. Fluid Mech.* **831**, 1 (2017).
- [31] I. Lozovatsky and H. J. Fernando, Mixing efficiency in natural flows, *Philos. Trans. R. Soc. A* **371**, 20120213 (2013).
- [32] D. Bouffard and L. Boegman, A diapycnal diffusivity model for stratified environmental flows, *Dyn. Atmos. Oceans* **61–62**, 14 (2013).
- [33] M. E. Barry, G. N. Ivey, K. B. Winters, and J. Imberger, Measurements of diapycnal diffusivities in stratified fluids, *J. Fluid Mech.* **442**, 267 (2001).
- [34] A. Maffioli, G. Brethouwer, and E. Lindborg, Mixing efficiency in stratified turbulence, *J. Fluid Mech.* **794**, R3 (2016).
- [35] G. D. Portwood, S. M. de Bruyn Kops, and C. P. Caulfield, Asymptotic Dynamics of High Dynamic Range Stratified Turbulence, *Phys. Rev. Lett.* **122**, 194504 (2019).
- [36] A. Garanaik and S. K. Venayagamoorthy, On the inference of the state of turbulence and mixing efficiency in stably stratified flows, *J. Fluid Mech.* **867**, 323 (2019).
- [37] C. J. Howland, J. R. Taylor, and C. P. Caulfield, Mixing in forced stratified turbulence and its dependence on large-scale forcing, *J. Fluid Mech.* **898**, A7 (2020).
- [38] V. Issaev, N. Williamson, S. W. Armfield, and S. E. Norris, Parameterization of mixing in stratified open channel flow, *J. Fluid Mech.* **935**, A17 (2022).
- [39] J. Tu, D. Fan, Z. Liu, and W. Smyth, Scaling the mixing efficiency of sediment-stratified turbulence, *Geophys. Res. Lett.* **49**, e2022GL099025 (2022).
- [40] Y. R. Yi and J. R. Koseff, Dynamics and energetics underlying mixing efficiency in homogeneous stably stratified turbulence, *Phys. Rev. Fluids* **7**, 084801 (2022).
- [41] Y. R. Yi and J. R. Koseff, Revised mixing coefficient scaling for sheared stably stratified turbulence, *J. Fluid Mech.* **952**, A18 (2022).
- [42] H. Salehipour, C. P. Caulfield, and W. R. Peltier, Turbulent mixing due to the Holmboe wave instability at high Reynolds number, *J. Fluid Mech.* **803**, 591 (2016).
- [43] M. S. Davies Wykes, G. O. Hughes, and S. B. Dalziel, On the meaning of mixing efficiency for buoyancy-driven mixing in stratified turbulent flows, *J. Fluid Mech.* **781**, 261 (2015).
- [44] E. Bou-Zeid, X. Gao, C. Anson, and G. G. Katul, On the role of return to isotropy in wall-bounded turbulent flows with buoyancy, *J. Fluid Mech.* **856**, 61 (2018).
- [45] S. E. Holt, J. R. Koseff, and J. H. Ferziger, A numerical study of the evolution and structure of homogeneous stably stratified sheared turbulence, *J. Fluid Mech.* **237**, 499 (1992).
- [46] F. G. Jacobitz, S. Sarkar, and C. W. Van Atta, Direct numerical simulations of the turbulence evolution in a uniformly sheared and stably stratified flow, *J. Fluid Mech.* **342**, 231 (1997).
- [47] A. Mashayek and W. R. Peltier, Three-dimensionalization of the stratified mixing layer at high Reynolds number, *Phys. Fluids* **23**, 111701 (2011).
- [48] A. Mashayek and W. R. Peltier, The ‘zoo’ of secondary instabilities precursory to stratified shear flow transition. Part 1 Shear aligned convection, pairing, and braid instabilities, *J. Fluid Mech.* **708**, 5 (2012).
- [49] A. Mashayek and W. R. Peltier, The ‘zoo’ of secondary instabilities precursory to stratified shear flow transition. Part 2 The influence of stratification, *J. Fluid Mech.* **708**, 45 (2012).
- [50] H. Salehipour and W. R. Peltier, Deep learning of mixing by two ‘atoms’ of stratified turbulence, *J. Fluid Mech.* **861**, R4 (2019).

- [51] A. K. Kaminski and W. D. Smyth, Stratified shear instability in a field of pre-existing turbulence, *J. Fluid Mech.* **862**, 639 (2019).
- [52] A. VanDine, H. T. Pham, and S. Sarkar, Turbulent shear layers in a uniformly stratified background: DNS at high Reynolds number, *J. Fluid Mech.* **916**, A42 (2021).
- [53] S. F. Lewin and C. P. Caulfield, The influence of far field stratification on shear-induced turbulent mixing, *J. Fluid Mech.* **928**, A20 (2021).
- [54] A. K. Kaminski, E. A. D'Asaro, A. Y. Shcherbina, and R. R. Harcourt, High-resolution observations of the north Pacific transition layer from a Lagrangian float, *J. Phys. Oceanogr.* **51**, 3163 (2021).
- [55] K. M. Smith, C. P. Caulfield, and J. R. Taylor, Turbulence in forced stratified shear flows, *J. Fluid Mech.* **910**, A42 (2021).
- [56] C.-L. Liu, A. K. Kaminski, and W. D. Smyth, The butterfly effect and the transition to turbulence in a stratified shear layer, *J. Fluid Mech.* **953**, A43 (2022).
- [57] J. Olsthoorn, A. K. Kaminski, and D. M. Robb, Dynamics of asymmetric stratified shear instabilities, *Phys. Rev. Fluids* **8**, 024501 (2023).
- [58] B. Gayen and S. Sarkar, Boundary mixing by density overturns in an internal tidal beam, *Geophys. Res. Lett.* **38**, L14608 (2011).
- [59] B. Gayen and S. Sarkar, Negative turbulent production during flow reversal in a stratified oscillating boundary layer on a sloping bottom, *Phys. Fluids* **23**, 101703 (2011).
- [60] N. Williamson, S. W. Armfield, and W. Lin, Forced turbulent fountain flow behaviour, *J. Fluid Mech.* **671**, 535 (2011).
- [61] M. van Reeuwijk, M. Holzner, and C. P. Caulfield, Mixing and entrainment are suppressed in inclined gravity currents, *J. Fluid Mech.* **873**, 786 (2019).
- [62] Y. Onuki, S. Joubaud, and T. Dauxois, Simulating turbulent mixing caused by local instability of internal gravity waves, *J. Fluid Mech.* **915**, A77 (2021).
- [63] S. F. Lewin and C. P. Caulfield, Stratified turbulent mixing in oscillating shear flows, *J. Fluid Mech.* **944**, R3 (2022).
- [64] P. Billant and J.-M. Chomaz, Experimental evidence for a new instability of a vertical columnar vortex pair in a strongly stratified fluid, *J. Fluid Mech.* **418**, 167 (2000).
- [65] P. Billant and J.-M. Chomaz, Theoretical analysis of the zigzag instability of a vertical columnar vortex pair in a strongly stratified fluid, *J. Fluid Mech.* **419**, 29 (2000).
- [66] S. Basak and S. Sarkar, Dynamics of a stratified shear layer with horizontal shear, *J. Fluid Mech.* **568**, 19 (2006).
- [67] A. Deloncle, J.-M. Chomaz, and P. Billant, Three-dimensional stability of a horizontally sheared flow in a stably stratified fluid, *J. Fluid Mech.* **570**, 297 (2007).
- [68] M. L. Waite and P. K. Smolarkiewicz, Instability and breakdown of a vertical vortex pair in a strongly stratified fluid, *J. Fluid Mech.* **606**, 239 (2008).
- [69] P. Augier, P. Billant, and J.-M. Chomaz, Stratified turbulence forced with columnar dipoles: Numerical study, *J. Fluid Mech.* **769**, 403 (2015).
- [70] D. Lucas, C. P. Caulfield, and R. R. Kerswell, Layer formation in horizontally forced stratified turbulence: Connecting exact coherent structures to linear instabilities, *J. Fluid Mech.* **832**, 409 (2017).
- [71] L. Cope, P. Garaud, and C. P. Caulfield, The dynamics of stratified horizontal shear flows at low Péclet number, *J. Fluid Mech.* **903**, A1 (2020).
- [72] S. A. Thorpe, The excitation, dissipation, and interaction of internal waves in the deep ocean, *J. Geophys. Res.* **80**, 328 (1975).
- [73] J. A. MacKinnon, Z. Zhao, C. B. Whalen, A. F. Waterhouse, D. S. Trossman, O. M. Sun, L. C. St. Laurent, H. L. Simmons, K. Polzin, R. Pinkel, A. Pickering, N. J. Norton, J. D. Nash, R. Musgrave, L. M. Merchant, A. V. Melet, B. Mater, S. Legg, W. G. Large, E. Kunze *et al.*, Climate process team on internal wave-driven ocean mixing, *Bull. Am. Meteorol. Soc.* **98**, 2429 (2017).
- [74] C. Dhandapani, K. J. Rah, and G. Blanquart, Effective forcing for direct numerical simulations of the shear layer of turbulent free shear flows, *Phys. Rev. Fluids* **4**, 084606 (2019).
- [75] B. E. Launder, On the effects of a gravitational field on the turbulent transport of heat and momentum, *J. Fluid Mech.* **67**, 569 (1975).

- [76] P. A. Durbin and B. A. Pettersson Reif, *Statistical Theory and Modeling for Turbulent Flows*, 2nd ed. (Wiley, Chichester, 2011).
- [77] Z. Hao and C. Górlé, Pressure scrambling effects and the quantification of turbulent scalar flux model uncertainties, *Phys. Rev. Fluids* **5**, 082501(R) (2020).
- [78] M. M. Rogers, N. N. Mansour, and W. C. Reynolds, An algebraic model for the turbulent flux of a passive scalar, *J. Fluid Mech.* **203**, 77 (1989).
- [79] C. Canuto, A. Quarteroni, M. Y. Hussaini, and T. A. Zang, *Spectral Methods: Evolution to Complex Geometries and Applications to Fluid Dynamics* (Springer, Berlin, 2007).
- [80] C. Canuto, M. Y. Hussaini, A. Quarteroni, and T. A. Zang, *Spectral Methods: Fundamentals in Single Domains* (Springer, Berlin, 2006).
- [81] S. B. Pope, *Turbulent Flows* (Cambridge University Press, Cambridge, 2000).
- [82] L. H. Shih, J. R. Koseff, J. H. Ferziger, and C. R. Rehmann, Scaling and parameterization of stratified homogeneous turbulent shear flow, *J. Fluid Mech.* **412**, 1 (2000).
- [83] B. D. Mater and S. K. Venayagamoorthy, A unifying framework for parameterizing stably stratified shear-flow turbulence, *Phys. Fluids* **26**, 036601 (2014).
- [84] E. C. Itsweire, J. R. Koseff, D. A. Briggs, and J. H. Ferziger, Turbulence in stratified shear flows: Implications for interpreting shear-induced mixing in the ocean, *J. Phys. Oceanogr.* **23**, 1508 (1993).
- [85] C.-H. Moeng and J. C. Wyngaard, An analysis of closures for pressure-scalar covariances in the convective boundary layer, *J. Atmos. Sci.* **43**, 2499 (1986).
- [86] R. Heinze, D. Mironov, and S. Raasch, Analysis of pressure-strain and pressure gradient-scalar covariances in cloud-topped boundary layers: A large-eddy simulation study, *J. Adv. Model. Earth Syst.* **8**, 3 (2016).
- [87] M. Ding, K. X. Nguyen, S. Liu, M. J. Otte, and C. Tong, Investigation of the pressure-strain-rate correlation and pressure fluctuations in convective and near neutral atmospheric surface layers, *J. Fluid Mech.* **854**, 88 (2018).
- [88] B. C. Pearson, A. L. M. Grant, and J. A. Polton, Pressure-strain terms in Langmuir turbulence, *J. Fluid Mech.* **880**, 5 (2019).
- [89] G. L. Mellor and T. Yamada, Development of a turbulence closure model for geophysical fluid problems, *Rev. Geophys.* **20**, 851 (1982).
- [90] T. J. Craft, N. Z. Ince, and B. E. Launder, Recent developments in second-moment closure for buoyancy-affected flows, *Dyn. Atmos. Oceans Stratified Flows*, **23**, 99 (1996).
- [91] V. M. Canuto, A. Howard, Y. Cheng, and M. S. Dubovikov, Ocean turbulence. Part I: One-point closure model-momentum and heat vertical diffusivities, *J. Phys. Oceanogr.* **31**, 1413 (2001).
- [92] M. M. P. Couchman, B. Wynne-Cattanach, M. H. Alford, C. P. Caulfield, R. R. Kerswell, J. A. MacKinnon, and G. Voet, Data-driven identification of turbulent oceanic mixing from observational microstructure data, *Geophys. Res. Lett.* **48**, e2021GL094978 (2021).
- [93] A. Mashayek, C. P. Caulfield, and M. H. Alford, Goldilocks mixing in oceanic shear-induced turbulent overturns, *J. Fluid Mech.* **928**, A1 (2021).
- [94] G. G. Katul, A. Porporato, S. Shah, and E. Bou-Zeid, Two phenomenological constants explain similarity laws in stably stratified turbulence, *Phys. Rev. E* **89**, 023007 (2014).